

JGR Solid Earth



RESEARCH ARTICLE

10.1029/2022JB024098

Key Points:

- We use *interrogation theory* to answer specific questions about the subsurface using probabilistic tomography results
- In a synthetic example, the method estimates the area of a low velocity anomaly accurately, even given coarsely gridded tomographic images
- We apply the method to a real data set and evaluate the volume of the East Irish Sea sedimentary basins using 3D depth inversion results

Supporting Information:

Supporting Information may be found in the online version of this article.

Correspondence to:

X. Zhao,
xuebin.zhao@ed.ac.uk

Citation:

Zhao, X., Curtis, A., & Zhang, X. (2022). Interrogating subsurface structures using probabilistic tomography: An example assessing the volume of Irish Sea basins. *Journal of Geophysical Research: Solid Earth*, 127, e2022JB024098. <https://doi.org/10.1029/2022JB024098>

Received 24 JAN 2022
Accepted 7 APR 2022

Author Contributions:

Conceptualization: Xuebin Zhao
Funding acquisition: Andrew Curtis
Investigation: Xuebin Zhao, Xin Zhang
Methodology: Xuebin Zhao
Project Administration: Andrew Curtis
Supervision: Andrew Curtis
Validation: Xin Zhang
Writing – original draft: Xuebin Zhao
Writing – review & editing: Andrew Curtis

Interrogating Subsurface Structures Using Probabilistic Tomography: An Example Assessing the Volume of Irish Sea Basins

Xuebin Zhao¹ , Andrew Curtis¹ , and Xin Zhang¹ 

¹School of Geosciences, University of Edinburgh, Edinburgh, UK

Abstract The ultimate goal of a scientific investigation is usually to find answers to specific, often low-dimensional questions: what is the size of a subsurface body? Does a hypothesized subsurface feature exist? Existing information is reviewed, an experiment is designed and performed to acquire new data, and the most likely answer is estimated. Typically the answer is interpreted from geological and geophysical data or models, but is biased because only one particular forward function is considered, one inversion method is applied, and because human interpretation is a biased process. Interrogation theory provides a systematic way to answer specific questions by combining forward, design, inverse, and decision theories. The optimal answer is made more robust since it balances multiple possible forward models, inverse algorithms and model parametrizations, probabilistically. In a synthetic test, we evaluate the area of a low-velocity anomaly by interrogating Bayesian tomographic results. By combining the effect of four inversion algorithms, the optimal answer is very close to the true answer, even on a coarsely gridded parametrization. In a field data test, we evaluate the volume of the East Irish Sea basins using probabilistic 3D shear wave speed depth inversion results. This example shows that interrogation theory provides a useful way to answer realistic questions about the Earth. A key revelation is that while the majority of computation may be spent solving inverse problems, much of the skill and effort involved in answering questions may be spent defining and calculating target function values in a clear and unbiased manner.

Plain Language Summary This paper shows how to answer specific questions about the subsurface using probabilistic tomography. Usually tomographic methods are used to estimate images of the subsurface; the “best” images are then interpreted to answer questions of interest. This work shows that by setting up a formal target function that allows any image to be interpreted automatically, many samples of possible subsurface models can be translated into probabilistic answers to the questions, from which a least-biased answer can be constructed. In the real-data examples presented here the subsurface shape of a sedimentary basin is determined automatically, and a least-biased estimate of its volume is constructed. This method is shown to give accurate answers about high resolution structures even given only low resolution tomographic images; this suggests that the probabilistic results compensate for the lack of resolution.

1. Introduction

Scientific investigations are usually initiated to answer high-level questions posed by investigators. Answers to these questions often lie within low-dimensional spaces: what is the depth of the Moho beneath a particular location? What is the best location to place a new sensor given locations of preexisting sensors? Can this subsurface aquifer be used for carbon storage? The answers to each of these questions are binary (yes/no) or low-dimensional (Moho depth or sensor location), yet they may depend on high-dimensional parameter spaces, describing the structure of Earth's subsurface for example. We usually seek answers using information that we know already - so-called *prior* information, and to better constrain the answer we collect new data. This involves designing an experiment, acquiring new data by experimentation, and interpreting the data to produce new and useful information. Finally the question is answered by taking both the prior information and the information from new data into account.

More formally, the new data is used to solve a Bayesian inverse problem in which we update the prior information with new information from the data, and seek to describe the resultant state of information by a probability distribution (Tarantola, 2005). Generally, inversion methods can be divided into two categories: linearized and nonlinear methods. The former iteratively approximates the possibly complex and nonlinear model-data

© 2022. The Authors.

This is an open access article under the terms of the [Creative Commons Attribution License](https://creativecommons.org/licenses/by/4.0/), which permits use, distribution and reproduction in any medium, provided the original work is properly cited.

relationship (the *forward* function) by a linear relationship, after which the inverse problem can be solved by minimizing a predefined objective function that measures the misfit between the observed data and synthetic data simulated from any given Earth model (Jackson, 1972). This kind of method requires a good initial model to avoid converging to local minima. In addition, it is not known how to estimate uncertainty or probability robustly from linearized inversion results, which means that we fail to find the solution to the Bayesian inverse problem. This in turn introduces bias when we use the results to answer questions of interest.

In contrast to linearized methods, fully nonlinear inversion methods solve the inverse problems under a probabilistic framework. They estimate or characterize the full probabilistic inversion results that describe all information about model parameters given the data - the so-called *posterior* probability distribution or density function (pdf). Such problems are often solved using Markov chain Monte Carlo (MCMC), which generates an ensemble of samples of the posterior distribution that fit the observed data to within measured data uncertainties. Many different kinds of MCMC methods have been introduced for geophysical inversion, for example: Metropolis Hastings MCMC (MH-MCMC; Mosegaard & Tarantola, 1995), reversible jump MCMC (Rj-MCMC; Bodin & Sambridge, 2009; Bodin et al., 2012; Galetti et al., 2015, 2017; X. Zhang et al., 2018), Hamiltonian Monte Carlo (HMC) (Fichtner et al., 2019; Fichtner & Simuté, 2018; Gebraad et al., 2020), informed proposal Monte Carlo (Khoshkholgh et al., 2021), and so on. All of these methods become very expensive when dealing with high-dimensional inference problems due to the curse of dimensionality (Curtis & Lomax, 2001). In an attempt to improve the computational efficiency, some approaches have been proposed to solve nonlinear Bayesian inverse problems using an optimization framework. These include neural network (NN) inversion (Devilee et al., 1999; Earp & Curtis, 2020; Käufel et al., 2014, 2016; Meier et al., 2007; Siahkoohi, Rizzuti, & Herrmann, 2021; Singh et al., 2021) and variational inference (Nawaz & Curtis, 2018, 2019; Nawaz et al., 2020; Siahkoohi, Orozco, et al., 2021; Siahkoohi, Rizzuti, Louboutin, et al., 2021; Zhang & Curtis, 2020a; Zhang et al., 2021; Zhao et al., 2021). However, the relative efficiency of all of the above methods depends on the problem at hand (Wolpert & Macready, 1997).

The probabilistic results of the inverse problem can be used to answer questions. For nonlinear inversion, a common way to achieve this is to interpret the mean model. For example, if we wish to estimate the size of a subsurface structure or feature using Bayesian tomographic inversion results, an intuitive way to proceed is to estimate its size using the mean seismic velocity map. However, answering questions using the mean model alone can be inaccurate since the mean model is only a single statistic of the posterior distribution and may not even represent a model that fits the observed data. In addition, human interpretation is a biased process, which sometimes leads to incorrect answers as shown in an example below. Since uncertainty in the result of the inverse problem is not considered, we cannot estimate uncertainty in the answers. Indeed, most of the information within the posterior distribution is summarily discarded when answering questions in this manner, which is extremely wasteful considering the computational cost of Bayesian inversion in nonlinear problems.

To address the above deficiencies, we suggest to answer questions using *interrogation theory*, a structured framework to design scientific investigations (Arnold & Curtis, 2018). It combines inverse theory, decision theory, and the theory of experimental design to optimize scientific investigations so as to find information that best answers scientific questions of interest. In this paper, we test one component of interrogation theory on real data, by using Bayesian nonlinear inversion results from multiple algorithms and parametrizations to answer a specific type of question: *what is the size of a near-surface geological body?* In our test the result is compared to the answer estimated from surface geological mapping. We then apply the method to assess the volume of a sedimentary basin, for which no independent estimate exists.

The rest of this paper is organized as follows. In the next section, we summarize the key components of interrogation theory and how we augment that theory in this paper, and show how optimal answers may be derived using Bayesian inversion results. In Section 3, we establish a detailed interrogation procedure using a synthetic example which estimates the area of a subsurface low velocity body based on probabilistic tomographic results. By using a coarse grid parametrization, we show that human interpretation can be significantly in error, yet in the same case the answer provided by interrogation theory remains accurate. In Section 4, we use interrogation theory to answer two real-world questions about the East Irish Sea sedimentary basins. Finally, we provide a brief discussion about this work and draw conclusions.

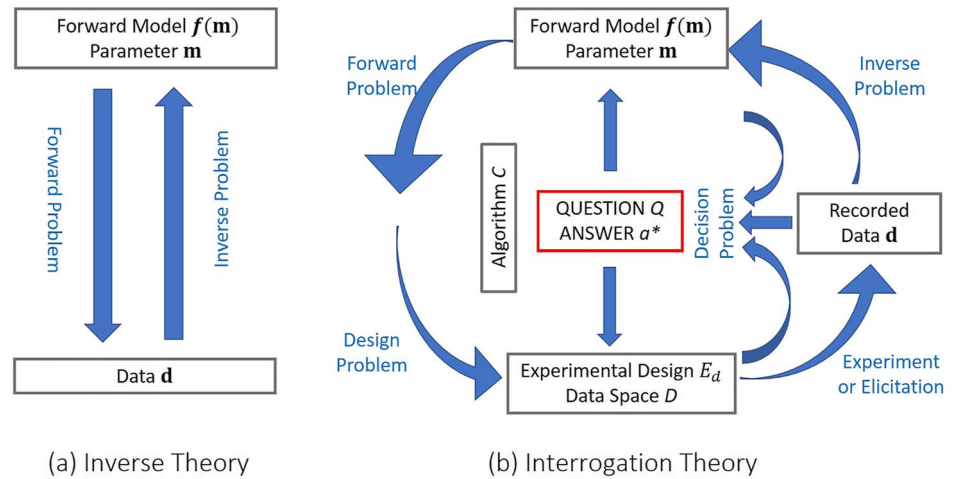


Figure 1. Comparison between inverse theory and interrogation theory. (a) Inverse theory: given observed data \mathbf{d} , we estimate model parameter \mathbf{m} . This is accomplished by evaluating the data match between the observed data and synthetic data simulated by solving a forward problem $f(\mathbf{m})$. (b) Interrogation theory: given a scientific question or a set of questions Q , we wish to find the optimal answer a^* . Forward, design, inverse, and decision problems are solved together to maximize information about the answer to question Q , rather than about parameter \mathbf{m} . In addition, in this paper the effect of different computational algorithms C for solving these problems is considered to reduce the bias of the final answer.

2. Theory

2.1. Bayesian Inverse Theory

Inverse theory is used to estimate the vector model parameter \mathbf{m} given some observed data \mathbf{d} , as shown in Figure 1a. This usually includes solving a forward problem that generates synthetic data corresponding to any parameter \mathbf{m} using a predefined *forward* function $f(\mathbf{m})$. The parameter space is then explored to find values that match the observed data to within their uncertainties. In a Bayesian framework, the inverse problem is solved in a probabilistic way by evaluating the so-called *posterior* probability density function (pdf) $p(\mathbf{m}|\mathbf{d})$ —the probability of model parameter \mathbf{m} given observed data \mathbf{d} —using Bayes' theorem:

$$p(\mathbf{m}|\mathbf{d}) = \frac{p(\mathbf{d}|\mathbf{m})p(\mathbf{m})}{p(\mathbf{d})} \quad (1)$$

Here, $p(\mathbf{m})$ is the *prior* pdf of model parameter \mathbf{m} , that is, the information we know about \mathbf{m} prior to the inversion. The conditional probability $p(\mathbf{d}|\mathbf{m})$ is the *likelihood* of observing data \mathbf{d} given a particular set of values for parameter vector \mathbf{m} , and is used to measure how consistent are the sample and the data. In the denominator, $p(\mathbf{d})$ is a normalization constant called the *evidence*.

MCMC is often used to solve Bayesian inference problems by sampling from the posterior distribution directly, yet it is often highly, if not impossible, expensive to sample it with representative density due to the curse of dimensionality (Curtis & Lomax, 2001). As an alternative, variational inference solves Bayesian inversion using an optimization framework by seeking the best approximation to the posterior distribution. This can be accomplished by minimizing the Kullback-Leibler (KL) divergence (Kullback & Leibler, 1951) between the approximated (so-called variational) distribution and the posterior distribution (Bishop, 2006; Blei et al., 2017; C. Zhang et al., 2018; Nawaz & Curtis, 2018, 2019; Nawaz et al., 2020; Siahkoohi, Rizzuti, & Herrmann, 2021; Siahkoohi, Rizzuti, Louboutin, et al., 2021; Zhang & Curtis, 2020a; Zhang et al., 2021; Zhao et al., 2021). In this work we combine results from both Monte Carlo and variational algorithms C .

2.2. Interrogation Theory

2.2.1. Fundamentals

Figure 1b outlines the key components of an interrogation problem, and a more detailed algorithmic flow chart is illustrated in Figure 2. Rather than focusing on the model parameter \mathbf{m} in an inverse problem, interrogation theory

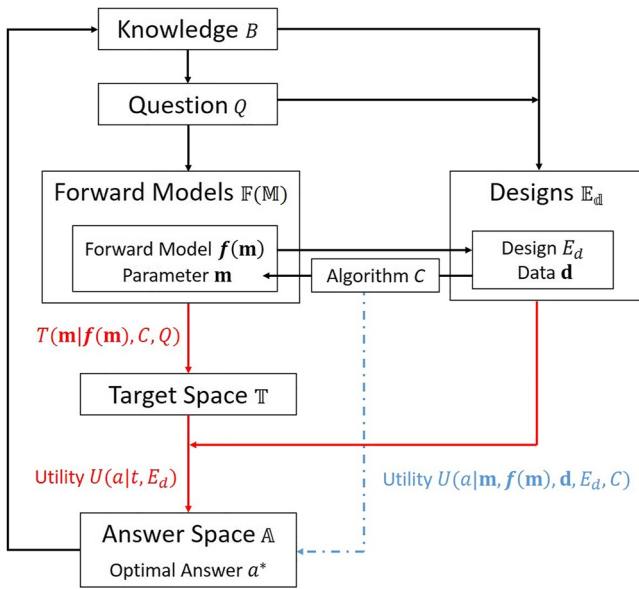


Figure 2. Algorithmic flow chart for interrogation theory. Given background knowledge B and a scientific question Q , we define forward model $f(\mathbf{m})$, the corresponding parameter \mathbf{m} , and experimental design E_d to collect new data \mathbf{d} . An inverse problem is solved to update the model parameter \mathbf{m} using the acquired data \mathbf{d} . In this paper, we solve inverse problems with different inversion algorithms $C \in \mathbb{C}$ and combine these results to reduce the bias that may occur from choosing one specific algorithm. A utility function U is constructed and further maximized to obtain the optimal answer a^* . The blue dashed lines show one way to define the utility function by combining all of the above elements directly, which is usually hard to achieve in reality. Instead, we introduce a target space \mathbb{T} and define a target function $T(\mathbf{m}|f(\mathbf{m}), C, Q)$ to simplify the utility function $U(a|t, E_d)$, as shown by the red lines.

orientates all theory around a scientific question Q and corresponding optimal answer a^* , which usually lies in a low-dimensional space \mathbb{A} . For example, geoscientists may be interested in the volume of a particular subsurface reservoir; the answer to this question would be a (one-dimensional) positive number. For other cases we may pose a binary question such as: is there a geothermal plume beneath this area? The answer would be yes or no. Since low-dimensional answers often lie within high-dimensional model parameters, which are constrained by high-dimensional data, it is hard to interpret data and answer questions directly. Interrogation theory provides a systematic way to investigate optimal answers to those questions.

As illustrated in Figure 2, at the beginning of an interrogation problem, investigators pose a question Q of interest given some background knowledge B . To answer this question, we first define a space of forward models $\mathbb{F}(\mathbb{M})$ in which all of the forward functions are deemed relevant to the question Q . Each element $f(\mathbf{m})$ maps parameter space into corresponding data space, and has a prior density functional $p(f(\mathbf{m}))$ which states the probability that this specific forward function $f(\mathbf{m})$ would accurately represent the parameter-data relationship. The set of forward models satisfies: $\sum_{f \in \mathbb{F}} p(f(\mathbf{m})) = 1$, assuming that the space of forward function is discrete. For each forward model, we define the corresponding model parameter \mathbf{m} and its prior probability distribution $p(\mathbf{m}|f(\mathbf{m}))$ such that $\int_{\mathbf{m}} p(\mathbf{m}|f(\mathbf{m})) d\mathbf{m} = 1$ where the integration is over the entire parameter space. For example, assume we are facing a seismic tomography related project. In this project, we use the following two forward functions to map subsurface velocity structure \mathbf{m} into corresponding first arrival travel time data \mathbf{d} between sources and receivers: ray tracing ($f_1(\mathbf{m})$ —Julian & Gubbins, 1977) and the fast marching method ($f_2(\mathbf{m})$ —Rawlinson & Sambridge, 2004). Since the former may fail to find the shortest travel time (the correct raypath) and is not robust for complex velocity structures, whereas the latter is capable of predicting travel times accurately in complex media, we assign prior probability density for these two forward functions as $p(f_1(\mathbf{m})) = 0.2$ and $p(f_2(\mathbf{m})) = 0.8$, respectively. For both forward functions, we use the same Uniform distribution to define our prior information on model parameter \mathbf{m} .

To answer question Q , we usually need some additional information, which is obtained by collecting new data. Given a set of forward models $f(\mathbf{m})$, an experimental design problem is solved to select the optimal design E_d to acquire data, selected from the space of designs \mathbb{E}_d . The difference between the design problem mentioned here and traditional experimental design problems (e.g., Maurer et al., 2010) is that the former finds a design that is chosen to provide the most relevant information to answer question Q , whereas the latter finds a design that best constrains model parameter \mathbf{m} . After implementing the experiment, the recorded data is used to update information about model parameter \mathbf{m} by solving an inverse problem, after which we can answer question Q .

Usually a variety of different computational algorithms can be used to solve forward, design, and inverse problems. These may provide significantly different solutions. For example, Zhao et al. (2021) illustrated that different results were obtained when solving the same Bayesian tomographic problem with four different inversion algorithms. Choosing any one of those results is likely to bias any inferred answer to question Q . To reduce bias in the optimal answer, in this paper we account for uncertainties due to the variety of computational algorithms $C \in \mathbb{C}$ (where \mathbb{C} is a space that contains all possible algorithms that might solve the inverse problem at hand), augmenting the original interrogation framework outlined in Arnold and Curtis (2018).

We define a utility function $U(a)$, which quantifies the net benefits of accepting any particular answer a . The utility is defined such that the optimal answer a^* that maximizes the utility function is the one that best satisfies whatever properties we require of our answer (Chaloner & Verdinelli, 1995): $a^* = \underset{a \in \mathbb{A}}{\text{argmax}} U(a)$. Figure 2 shows two approaches to construct the utility function. In the first, we combine all of the information provided in the components of interrogation problems described above, to define a highly structured utility function: $U(a|\mathbf{m},$

$f(\mathbf{m}), \mathbf{d}, E_d, C$) as illustrated by dashed blue lines in Figure 2. Note that this utility function is conditioned on the data \mathbf{d} and experimental design E_d to account for the cost of conducting the experiment given a specific design or to allow the data to provide some components of answer a directly (Arnold & Curtis, 2018). However, the investigator may in general have no means of constructing a utility function of such structure and complexity. Moreover, even when agreeing to a utility function with such a high dimensional set of independent variables, an investigator cannot generally be expected to appreciate all of the consequences of choosing a specific functional form (Curtis & Lomax, 2001). Also, there is no straightforward way to maximize this utility function over the usually discrete choices of forward functions and algorithms under consideration. As an alternative, Arnold and Curtis (2018) introduced a target space \mathbb{T} which is determined by question Q such that Q can be answered directly in \mathbb{T} . The target space should be the same for all forward functions $f(\mathbf{m})$ and algorithms C . A target function $T(\mathbf{m}|f(\mathbf{m}), C, Q)$ is defined to convert the model parameter \mathbf{m} into a target value t . Based on this, a new utility function can be expressed as $U(a|t, E_d)$ which has a much simpler form since it is only conditioned on target value t and design E_d . Usually this is expected to be easier to maximize (shown by red lines in Figure 2).

As an example of a target function, below we will address the question Q , “What is the volume of a subsurface body?” We wish to answer this question using seismic tomographic results. The target function $T(\mathbf{m}|f(\mathbf{m}), C, Q)$ is defined to transform the model parameter \mathbf{m} —the subsurface velocity structure in this case—into the corresponding volume of the subsurface body of interest. Thus, the target function maps a high-dimensional parameter space into a low-dimensional target space, eliminating nuisance parameters and retaining only information that is essential to represent the answer to the question. For more details about interrogation theory and these components, we refer readers to Arnold and Curtis (2018).

2.2.2. The Optimal Answer

In this paper, we use the same utility function defined in Arnold and Curtis (2018)—a negative squared error function:

$$U(a|t, E_d) = U(a|t) = -(a - t)^2 \quad (2)$$

in which t is assumed to be the true summarized state of nature in the target space. The utility function in Equation 2 is maximized when the estimated answer a is equal to (or is as close as possible to) state t . This results in an analytical solution of the optimal answer a^* : the posterior mean of $T(\mathbf{m}|f(\mathbf{m}), C, Q)$ averaged over all $\mathbf{m}, f(\mathbf{m})$, and C :

$$\begin{aligned} a^* &= \mathbb{E}[T(\mathbf{m}|f(\mathbf{m}), C, Q)|\mathbf{d}, E_d] \\ &= \sum_{f(\mathbf{m}), C} \int_{\mathbf{m}} T(\mathbf{m}|f(\mathbf{m}), C, Q) p(\mathbf{m}, f(\mathbf{m}), C|\mathbf{d}, E_d) d\mathbf{m} \\ &= \sum_{f(\mathbf{m}), C} p(C, f(\mathbf{m})) \int_{\mathbf{m}} T(\mathbf{m}|f(\mathbf{m}), C, Q) p(\mathbf{m}|f(\mathbf{m}), \mathbf{d}, E_d, C) d\mathbf{m} \\ &= \sum_{f(\mathbf{m}), C} p(f(\mathbf{m})) p(C|f(\mathbf{m})) \int_{\mathbf{m}} T(\mathbf{m}|f(\mathbf{m}), C, Q) p(\mathbf{m}|f(\mathbf{m}), \mathbf{d}, E_d, C) d\mathbf{m} \end{aligned} \quad (3)$$

where $p(\mathbf{m}|f(\mathbf{m}), \mathbf{d}, E_d, C)$ is the probability of model parameter \mathbf{m} given a specific forward function $f(\mathbf{m})$, observed data \mathbf{d} , design E_d and algorithm C , describing the posterior distribution of model parameter \mathbf{m} in Bayesian inversion. Integration in the third line $\int_{\mathbf{m}} T(\mathbf{m}|f(\mathbf{m}), C, Q) p(\mathbf{m}|f(\mathbf{m}), \mathbf{d}, E_d, C) d\mathbf{m}$ calculates the optimal answer given a specific forward model $f(\mathbf{m})$ and computational algorithm C (denoted as $a_{f(\mathbf{m}), C}^*$ below). The third line of Equation 3 holds based on the assumption that forward model $f(\mathbf{m})$ and algorithm C are usually independent of design E_d and observed data \mathbf{d} . Then, term $p(C, f(\mathbf{m})) = p(f(\mathbf{m})) p(C|f(\mathbf{m}))$ describes the joint probability density of forward function $f(\mathbf{m})$ and algorithm C , where $p(C|f(\mathbf{m}))$ is the prior probability that a specific algorithm C will find the correct solution given that forward function $f(\mathbf{m})$ does adequately describe the forward physics. Note that C and $f(\mathbf{m})$ are not necessarily independent of each other since some forward functions may preclude the use of different algorithms. For example, we would prefer to use Monte Carlo sampling method if the forward function can be solved cheaply, since the algorithm provides an unbiased approximation of the true solution of a Bayesian inversion problem only as the number of samples becomes large. Therefore we would not consider this algorithm when the forward function is incredibly expensive (e.g., a full waveform simulator that solves the 3D wave equation). Equation 3 states that the final optimal answer a^* is a weighted sum of $a_{f(\mathbf{m}), C}^*$ over all of the models and algorithms considered. This can be understood intuitively: by considering the effect

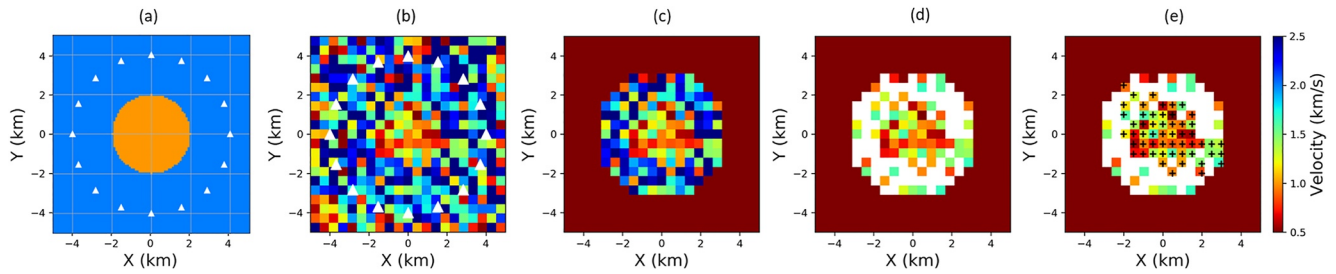


Figure 3. (a) True velocity model used for the 2D synthetic example. (b) A random sample drawn from the posterior distribution of Metropolis Hastings Markov chain Monte Carlo. (c) The same sample in (b) after applying the mask defined in the main text. (d) The retained low velocity pixels after comparing the velocity of every pixel in (c) with the optimal threshold value. (e) Black crosses mark the largest spatially continuous low velocity body in (d). The target function calculates the area of this body.

of different forward models and algorithms, we reduce the bias due to subjective choices and so obtain a more robust interrogation result.

To conclude, Equation 3 answers question Q by interrogating the Bayesian inversion results. It also shows that a design E_d that provides optimal answers to question Q would potentially be very different from one designed to maximize information in the posterior distribution $p(\mathbf{m}|f(\mathbf{m}), \mathbf{d}, E_d, C)$ as has been performed in previous research on geophysical optimal design (e.g., Bloem et al., 2020; Guest & Curtis, 2009; van Den Berg et al., 2003).

3. Implementation

3.1. Problem Statement

Interrogation theory described above can be used to answer many types of real-world questions. In this paper, we provide a specific application to answer volume-related (3D), area-related (2D), or other shape-related questions about a body or medium of interest using fully nonlinear tomographic results. This kind of question appears frequently in both academia and industry where we wish to interpret some geological phenomena from geophysical imaging results, such as to estimate the size of a subsurface body, the volume of a reservoir, or the depth of a particular feature such as the Moho under a specific location.

In this section, we use a 2D synthetic example to establish an interrogation procedure for estimating the area of a 2D subsurface body. Figure 3a shows the true velocity model used in this example: a circular low velocity anomaly of 1 km/s is discretized on a grid size of 0.1 km, and located at the center of the model, and its surrounding area has a high velocity value of 2 km/s. White triangles display the location of 16 receivers (equivalently 16 virtual sources) to collect traveltime data. Given only seismic travel time data from waves that traverse this velocity model, we pose a scientific question: what is the area of the low velocity anomaly?

3.2. Interrogation Procedure

Table 1 summarizes some key elements defined for this interrogation problem. We use the fast marching method (FMM) to represent the model-data relationship. Since this is the only forward model considered in this example, it has a prior probability $p(f(\mathbf{m})) = 1$. The corresponding model parameter \mathbf{m} is the subsurface seismic velocity structure using a regularly gridded parametrization, and a Uniform prior distribution is used for the velocity in each cell. To answer the question, we use an experimental design (i.e., source and receiver locations) that contains 16 receivers placed in a circular shape with a radius of 4 km around the low velocity area, as shown by the white triangles in Figure 3a, such that the collected data provides relevant information about the low velocity anomaly. These receivers are also treated as sources, to emulate the use of standard inter-receiver interferometry to provide source to receiver traveltimes (Curtis et al., 2006; Shapiro et al., 2005). Given the collected traveltime data, we solve a Bayesian inference problem to estimate the posterior distribution of the model parameter \mathbf{m} . We use four different algorithms to perform nonlinear Bayesian tomographic inversion: automatic differential variational inference (ADVI; Kucukelbir et al., 2017), normalizing flows (Rezende & Mohamed, 2015), Stein variational gradient descent (SVGD; Liu & Wang, 2016), and MH-McMC (Hastings, 1970; Metropolis et al., 1953; Metropolis & Ulam, 1949); each algorithm is described in Zhao et al. (2021), and the corresponding inversion results

Table 1
Key Interrogation Elements Defined for the Synthetic Test

Symbol	Meaning	Description
Q	Question	What is the area of the low velocity anomaly?
$f(\mathbf{m})$	Forward model	Fast marching method
\mathbf{m}	Parameter	Pixelated velocity structure with a Uniform prior pdf
E_d	Design	Source and receiver station locations
\mathbf{d}	Data	Source to receiver traveltimes
C	Algorithms	ADVI, Normalizing flows, SVGD and MH-McMC
$T(\mathbf{m})$	Target function	Transform \mathbf{m} into area of low velocity anomaly
$U(alt)$	Utility function	$-(a - t)^2$
a^*	Optimal answer	$\mathbb{E}[T(\mathbf{m}) f(\mathbf{m}), C, Q] \mathbf{d}, E_d]$

Note. ADVI, automatic differential variational inference; MH-McMC, Metropolis Hastings Markov chain Monte Carlo; SVGD, Stein variational gradient descent.

are shown in Figures 4a–4d. The top row of Figure 4 shows the (pixelated) mean velocity maps from the above four methods, while the bottom row shows the corresponding standard deviation maps. In this paper we will not focus on comparing the four inversion results as details about this inversion and a corresponding discussion can be found in Zhao et al. (2021). They concluded that (at least for seismic tomography problems that use FMM as the forward function $f(\mathbf{m})$) ADVI provides an accurate mean velocity model but a biased uncertainty estimation, and the other three methods give similar and accurate mean and uncertainty maps (the same conclusion can be reached by comparing Figure 4a to Figures 4b–4d). We wish to include the results from ADVI when we determine the optimal answer to the question since this method is relatively efficient and robust (in the sense that the result is highly repeatable), and the mean tends to be accurate in previous tests so it clearly provides information at relatively low computational cost. We downweight the contribution of this algorithm because of the bias expected in its uncertainty estimates by assigning it a relatively low prior probability: $p(C|f(\mathbf{m})) = 0.1$. For the other three algorithms, we assign equal prior values $p(C|f(\mathbf{m})) = 0.3$.

Based on the above elements, we define a target function that maps a posterior sample in high-dimensional parameter space into the area of the central low velocity anomaly in low-dimensional answer space. From the inversion results in Figures 4a–4d, the low velocity anomaly of interest is located close to the center of the model.

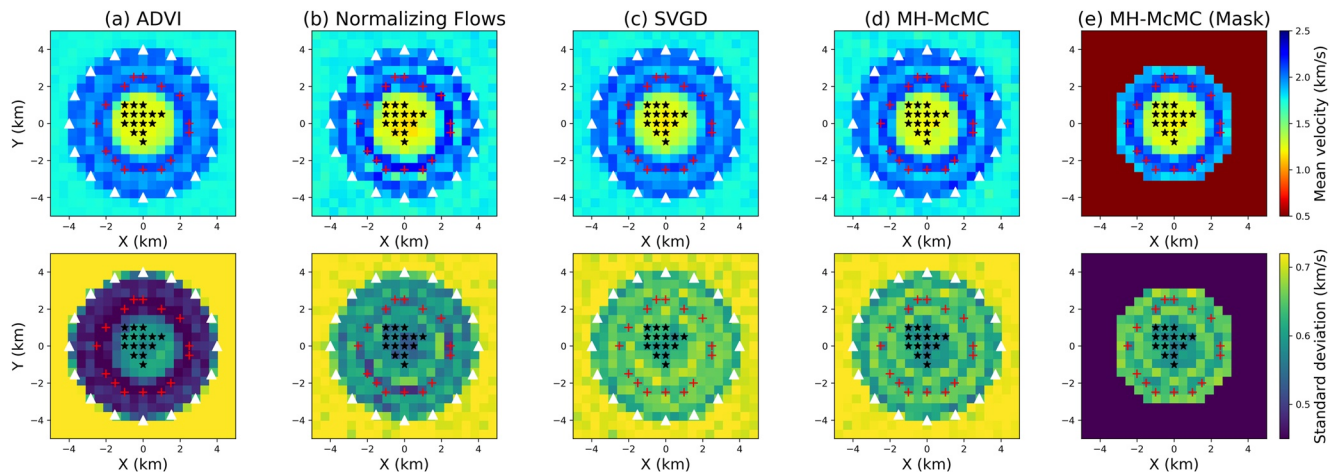


Figure 4. (a–d) Pixel-by-Pixel mean (top row) and standard deviation (bottom row) maps of the posterior distributions obtained using automatic differential variational inference (ADVI), normalizing flows, Stein variational gradient descent (SVGD), and Metropolis Hastings Markov chain Monte Carlo (MH-McMC). (e) The corresponding maps of MH-McMC in (d) after applying the mask introduced in the main text: only the remaining pixels are considered when estimating the area of the low velocity anomaly. White triangles in (a–d) illustrate the receiver (and source) locations of the experimental design. Red crosses and black stars in each figure denote the selected pixels used to define the threshold value to discriminate of low and high velocities.

Even though there might be some low velocity anomalies far from the central region, we assume that they have no relation with the central anomaly in which we are interested since they will be on or outside of the circular array of receivers. To encode this prior assumption, we introduce a mask to confine the region used to calculate the target function. Figure 4e illustrates the effect of the mask, which displays the mean and uncertainty maps of MH-McMC after applying the mask. The area outside of this mask is discarded, and only the remaining velocity pixels are retained to calculate the low velocity area. Thus the target function of each posterior sample $T(\mathbf{m}|f(\mathbf{m}), C, Q)$ becomes: the area of the low velocity anomaly inside the mask.

Figure 3b shows a posterior sample drawn from the inversion results of MH-McMC, and Figure 3c shows the same sample after applying the defined mask. One way to calculate the target function of this posterior sample is to sum up all of the area of low velocity pixels. This highlights a sub-question that must be answered in order to proceed: “what is the best threshold to discriminate low velocity from high velocity pixels with minimal bias?” If we could estimate such an optimal threshold value, we could classify each pixel as low or high velocity and hence calculate the target function value.

We define a data-driven way to obtain such a threshold value. First, we pick some pixels that are most likely to be high (and low) velocity cells from the four inversion results. Ideally, these pixels should have higher (lower) mean velocity values relative to the mean, and low uncertainties, as denoted by the red crosses (black stars) in Figure 4. A threshold value estimated from such pixels should represent high and low velocity information better than a value estimated using other, more ambiguous pixels, thus introducing minimal bias.

Figures 5a and 5b show marginal pdfs of the selected low and high velocity pixels, and Figures 5c and 5d display the corresponding marginal cumulative density functions (cdfs). Note that the low velocity marginal cdfs in Figure 5c are obtained by integrating the low velocity marginal pdfs in Figure 5a from low to high velocity (from left to right), whereas the high velocity cdfs in Figure 5d are obtained by integrating the marginal pdfs in Figure 5b in the opposite direction (from high to low velocity). We then average the marginal cdfs in Figures 5c and 5d and plot the averaged cdf curves in Figure 5e. The red line is the averaged cdf for low velocity pixels, and the blue line is that for high velocity pixels, and note that while these curves are close to being mirror images of each other this is not generally the case. The crossing point of the two lines is marked by the black dot with a velocity value of 1.676 km/s. This value is also illustrated by the dashed black line in each pdf curve in Figures 5a and 5b. This point has the property that the probability that the velocities of the selected low velocity pixels (black stars in Figure 4) are lower than this value equals the probability that the velocities of the selected high velocity pixels (red crosses in Figure 4) are higher than this value. This specific threshold value therefore discriminates low from high velocity values with minimal bias.

We compare the velocity value of each pixel in Figure 3c with the optimal threshold, and retain those whose velocity value is smaller than the threshold, as shown in Figure 3d. We interpret these pixels as low velocity bodies in this sample. Question Q demands the area of a single low velocity anomaly, rather than all of the low velocity pixels in Figure 3d. Therefore we add additional prior information that the low velocity anomaly of interest should represent a continuous geological body in space. Note that adding this information does not alter the original question Q ; rather it articulates the question more precisely. The question then becomes what is the area of the largest continuous low velocity body inside the mask, which for the sample in question is marked by black crosses in Figure 3e (continuity can occur through both laterally and diagonally adjacent pixels). Obviously this target function transforms a high-dimensional velocity vector \mathbf{m} into a (1-dimensional) scalar value, and eliminates nuisance parameters that are less relevant to the question, such that Q can be answered directly in the target space \mathbb{T} .

For each of the four inversion results we calculate the target function $T(\mathbf{m}|f(\mathbf{m}), C, Q)$ for every posterior sample, and plot the corresponding posterior histograms in Figure 6. Given the negative squared error utility function in Equation 2, the optimal answer for each algorithm a_c^* can be expressed as the posterior mean of target function $T(\mathbf{m}|f(\mathbf{m}), C, Q)$ (Equation 3), noted at the top-left corner and denoted by the dashed black line in Figure 6. We could further substitute these 4 results, their prior probability values $p(C|f(\mathbf{m}))$, and the prior probability of forward function $p(f(\mathbf{m})) = 1$ into Equation 3 to obtain the final optimal answer: 12.89 km²; this is very close to the true answer (12.56 km²) which is marked by red lines in Figure 6.

This example illustrates the accuracy of this interrogation procedure. Although the final answer is very close to (even slightly less accurate than) the answer obtained from normalizing flows (12.85 km²), we usually do not

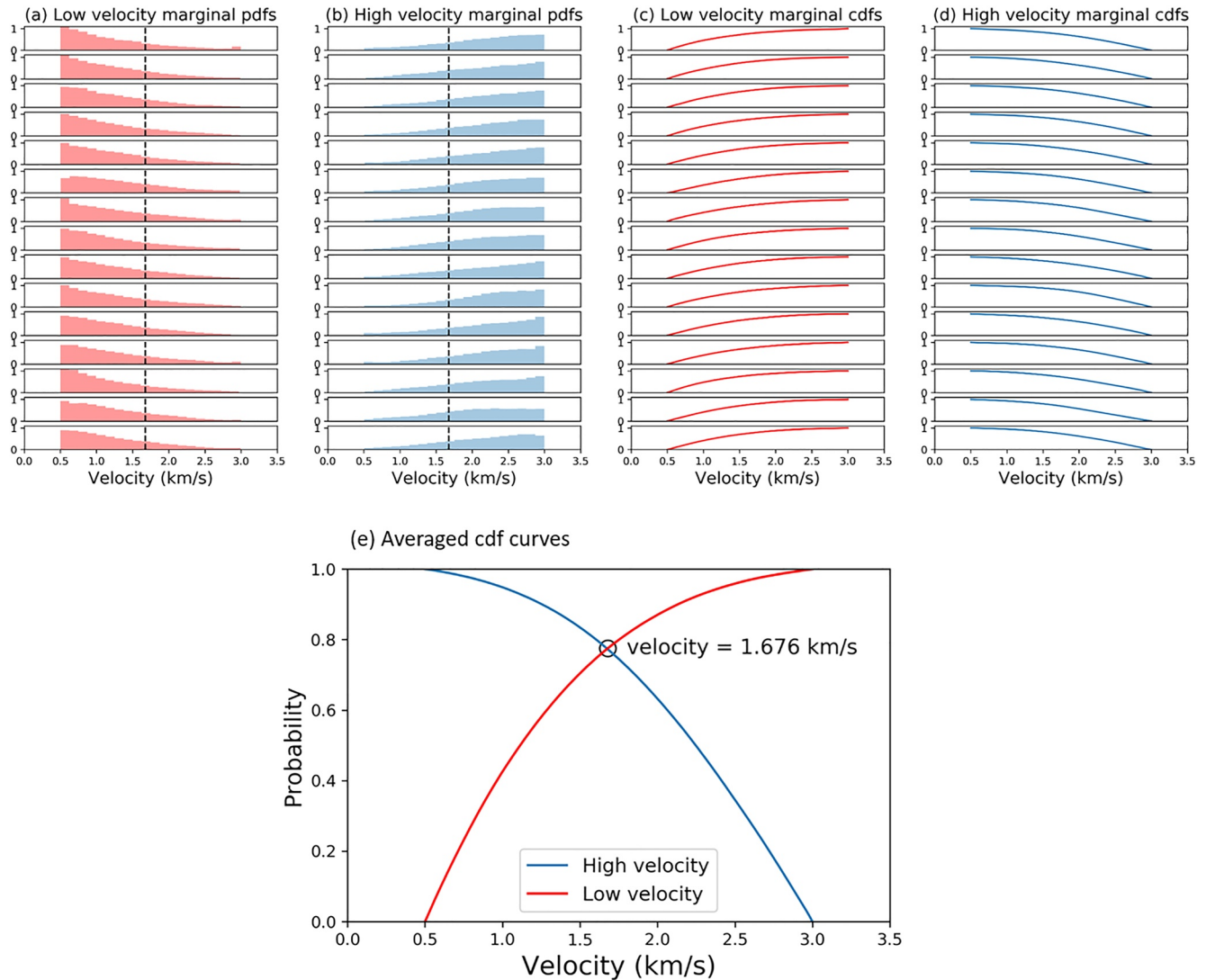


Figure 5. (a) and (b) Marginal probability density functions (pdfs) of low and high velocity marked in Figure 4. Dashed black lines denote the crossing point in (e), which is used to classify low and high velocity pixels. (c) and (d) Marginal cumulative density functions (cdfs) obtained by integrating the corresponding pdfs in (a) and (b) in opposite directions. (e) Averaged cdf curves for low (red line) and high (blue line) velocity pixels calculated using (c) and (d). Black dot marks the crossing point of the two curves, and is the threshold value that discriminates low from high velocities with minimal bias.

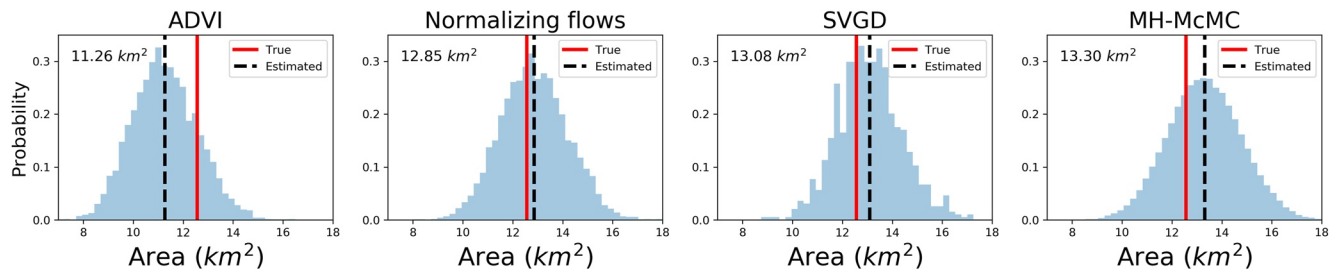


Figure 6. Posterior distributions of the target function for automatic differential variational inference (ADVI), normalizing flows, Stein variational gradient descent (SVGD), and Metropolis Hastings Markov chain Monte Carlo (MH-McMC), from left to right, respectively. The posterior mean value of each target function is displayed at the top-left corner, and is also marked by the dashed black line in each figure. The true answer to this question (12.56 km²) is denoted by the red lines.

know the true answer to our question for reference, and thus have no means to select the answer from one algorithm over any other. On the other hand, by considering the effect of different algorithms and by defining prior probabilities that each algorithm will provide the correct solution based on their past performance, we would be more confident about the final answer obtained.

Considering the true Earth has infinitely fine structure, whereas in reality we parametrize it with a finite (coarse) grid or number of parameters to reduce the dimensionality of our inverse problem, so it is crucial to consider the effect of different parametrizations when answering questions. In Supporting Information S1 associated with this article, we investigate the effect of interrogations carried out using models with different parametrizations. We double the grid size in both directions from 0.5 to 1 km, which decreases the dimensionality of the tomographic problem from 441 to 121. The results show that both the posterior histograms and their corresponding mean values from the coarser inversion results are quite similar to those obtained from the finer grid parametrization in Figure 6. The final answer of the coarser grid parametrization (12.37 km²) is very close to the true answer (12.56 km²), as well as that estimated from the finer grid parametrization (12.89 km²).

We thus obtain an accurate answer using interrogation theory using either parametrization. By contrast interpreting the mean map alone provides a severely erroneous answer (9 km²). This makes interrogation theory more attractive for answering scientific questions since we obtain an accurate answer to the question even under a coarse parametrization, which usually offers orders of magnitudes of computational cost reduction in real problems.

4. Interrogating the East Irish Sea Basins

4.1. Shear Wave Velocity Inversion of the East Irish Sea Basins

In the second example, we use interrogation theory to answer questions about the East Irish Sea sedimentary basins. Figure 7a displays 61 seismometer locations (red triangles) around the British Isles used in this test, all of which contain one vertical (Z) and two horizontal (North and East) components to detect ground motion. We consider ambient noise data recorded by these stations during 2001–2003, 2006–2007, and in 2010. Nicolson et al. (2014) cross-correlated the vertical component of the ambient noise data to estimate inter-receiver travel-times of Rayleigh waves, and to perform Rayleigh wave tomography of the British Isles. Galetti et al. (2017) used two horizontal components to calculate Love wave group velocity maps at different periods. A more detailed description about the ambient noise data and data processing can be found in Galetti et al. (2017). Since Love waves are dominantly sensitive to the near surface shear velocity structure, we perform shear wave group velocity depth inversion of the East Irish Sea basins using the estimated Love wave traveltimes measurements between 4 and 15 s periods, and interrogate the size of those sedimentary basins using the inversion results. Note that the receiver network used in this paper may not be the optimal experimental design to provide the most relevant information about the Irish Sea basins. However, it represents a common situation in seismology where we have fixed legacy designs, which are definitely not optimal for every question being posed, and nevertheless wish to find optimal answers to specific questions about the Earth.

We use a two-step scheme for the 3D shear wave group velocity depth inversion. In the first step, we perform Love wave tomography of the British Isles using inter-receiver traveltimes data at different periods of 4, 6, 8, 9, 10, 11, 12, and 15 s. For each period we perform 2D surface wave tomography, restricting the imaging region to within longitude 9°W – 3°E and latitude 48°N – 61°N, and parametrize the velocity model using a regular grid of 37 × 40 cells with a spacing of 0.33° in both longitude and latitude directions. The prior distribution is chosen to be a uniform distribution, and its lower and upper bounds are chosen according to Galetti et al. (2017). The likelihood function is chosen to be a Gaussian distribution, and the traveltimes data error of each inter-receiver path is estimated from daily cross-correlations (Galetti et al., 2017). Considering the dimensionality of this fully nonlinear inverse problem, we only use three variational methods: ADVI, normalizing flows, and SVGD to perform tomography at each period; we do not perform MH-McMC, as the results using that algorithm did not converge acceptably even after drawing 15 million samples in total with 10 chains using 660 hr of elapsed time (Zhao et al., 2021). Previously, Zhao et al. (2021) performed Love wave tomography at 10 s period to compare the performance of different algorithms. In this study, we run tomography at all periods and use these tomographic results to construct dispersion curves at each geographical location. These curves form the data set that is used to drive the depth inversion (more details on the latter are given below).

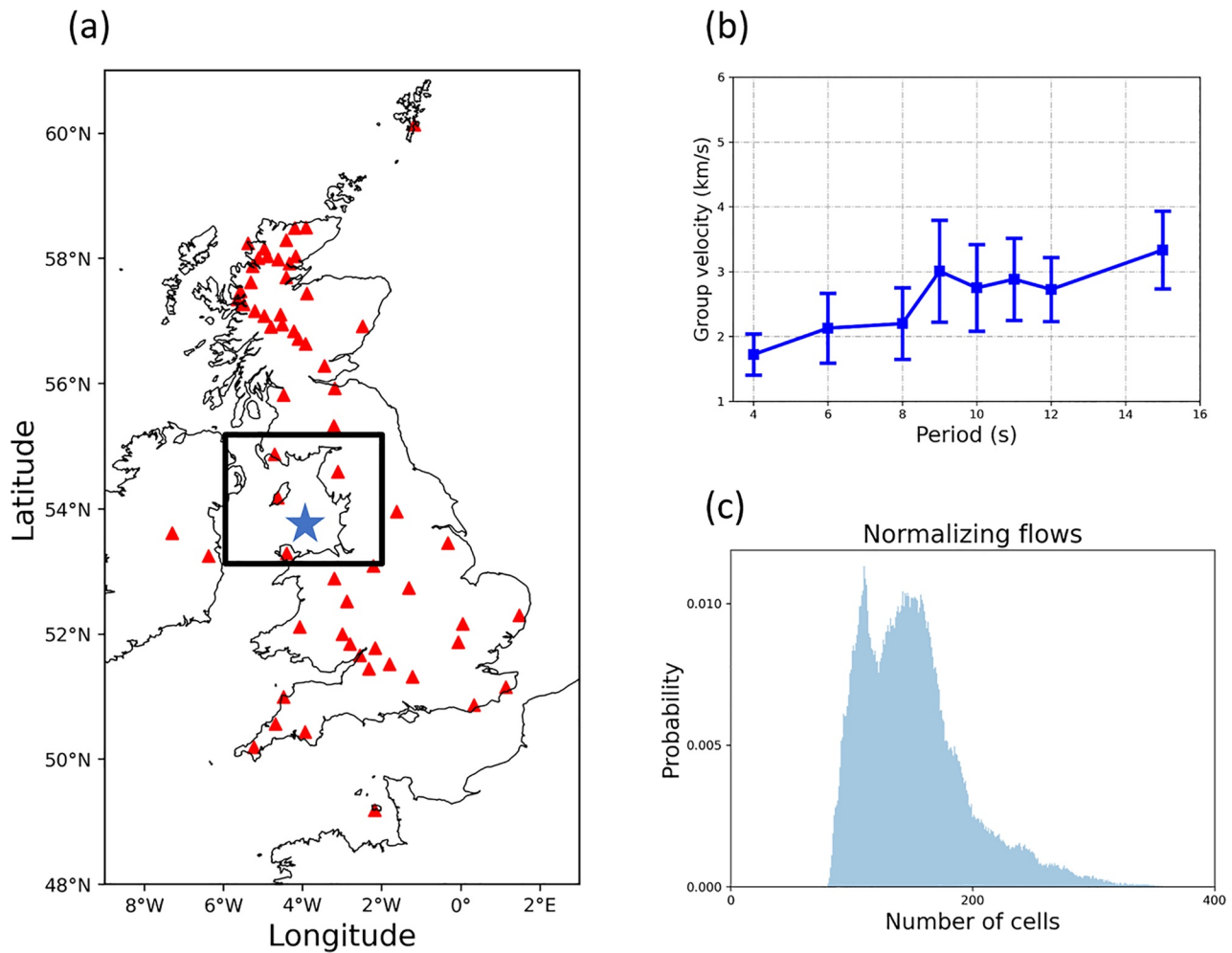


Figure 7. (a) The locations of 61 seismometers (red triangles) around the British Isles used in this paper to record ambient noise data. The recorded data were cross-correlated to provide inter-receiver traveltimes of Love waves at different periods of 4, 6, 8, 9, 10, 11, 12, and 15 s (Galetti et al., 2017). We use these data to perform shear wave group velocity depth inversion beneath the East Irish Sea within the black box, via a two-step scheme (see main text for details). (b) One dispersion curve picked from 2D tomographic inversion results of normalizing flows at the geographical point 4°W, 53.5°N, marked by the blue star in (a). (c) Posterior distribution on number of Voronoi cells.

Figure 8 shows average velocity maps of the Love wave tomography results using normalizing flows at all of the analyzed periods, and Figure 9 shows the corresponding uncertainty results. In order to aid the comparison of velocity structures and uncertainties between the various periods, the same color scales are used for all of the mean and standard deviation maps in Figures 8 and 9, respectively. Some small structures in Figures 8 and 9 are a bit different compared to those from reversible jump MCMC in Galetti et al. (2017) (which uses exactly the same traveltim data for Love wave group velocity tomography). This is due to different parametrizations used in the two studies: Galetti et al. (2017) used a variable parametrization using Voronoi cells to discretize the velocity model, whereas we use a fixed regularly-gridded parametrization. Nevertheless, the main features of the mean velocity and uncertainty maps show good consistency with the known geology and previous tomographic studies of the British Isles (Galetti et al., 2015, 2017; Nicolson et al., 2012, 2014). For example, from the tomographic results (especially at smaller periods which usually provide velocity information in the shallow subsurface), we observe a low velocity structure beneath the East Irish Sea within longitude 6°W–2°W and latitude 53°N – 55°N, marked by the black boxes in Figures 7a, 8, and 9. This low velocity anomaly corresponds to the East Irish sedimentary basins (Galetti et al., 2017).

In the second inversion step we focus on the East Irish Sea basins (inside the black box in Figure 7a) and perform dispersion inversion to estimate the 3D shear wave velocity structure at depth using the results from traveltim

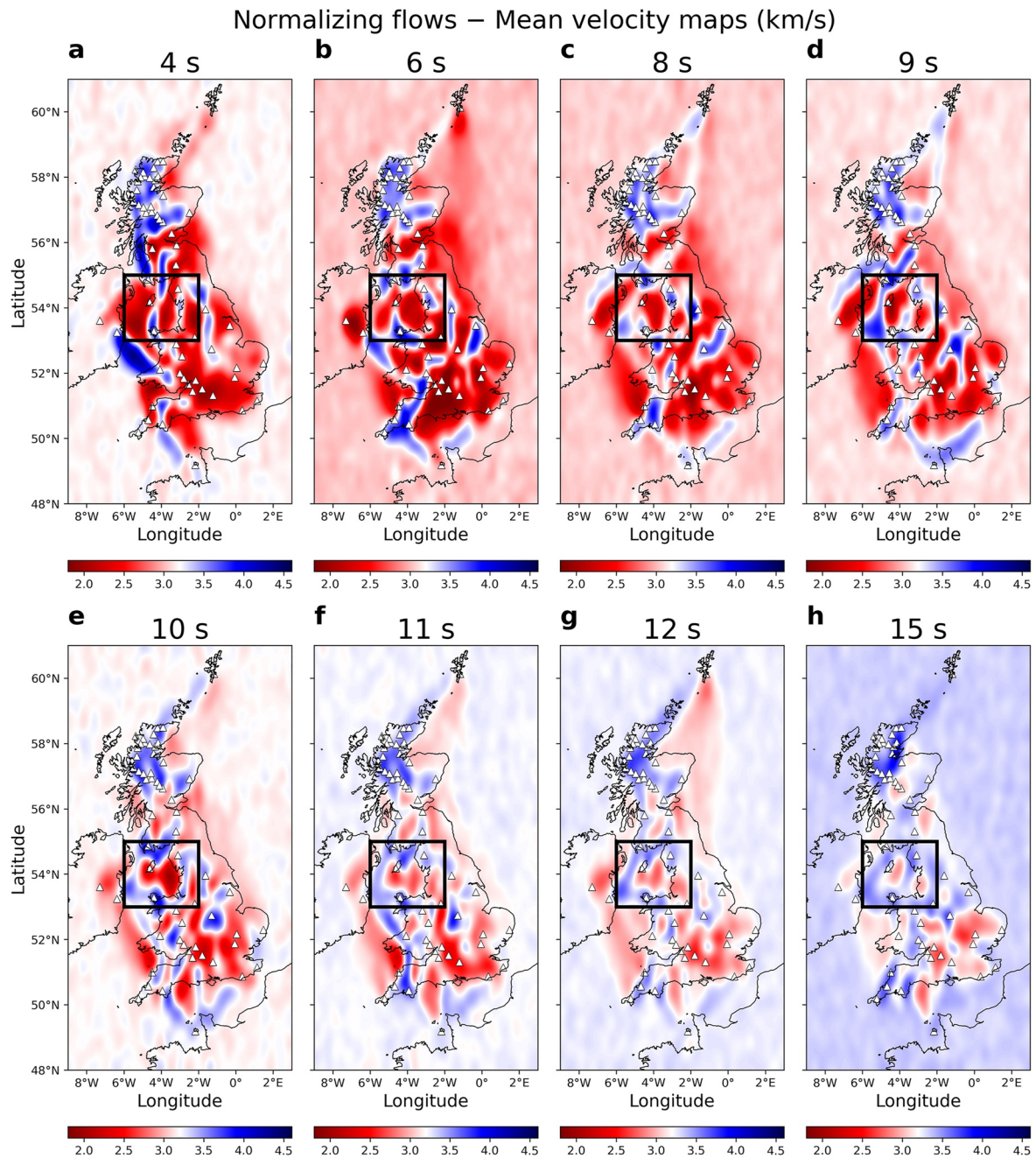


Figure 8. Mean Love wave group velocity maps of the British Isles, interpolated between grid cell locations in the results obtained using normalizing flows at different periods between 4 and 15 s. All of the mean maps are plotted using the same velocity range for better comparison, and the corresponding normalizing period is shown above each map. The black boxes indicate the target region where we pick dispersion curves and perform depth inversion in the second step.

tomography in the first step. To perform the depth inversion, we construct a data set of group velocity dispersion curves from the tomographic results. At each geographic point inside the black box in Figure 7a, a dispersion curve can be constructed by taking group velocity values from the 2D mean maps, and uncertainty values from the 2D standard deviation maps at each period. For example, Figure 7b shows one dispersion curve picked from the 2D tomography results in Figures 8 and 9 at 4°W, 53.5°N, the geographical location marked by the blue star in Figure 7a. Given the regular gridded parametrization scheme we used in the first step, we pick 91 dispersion curves inside the black box around the East Irish Sea.

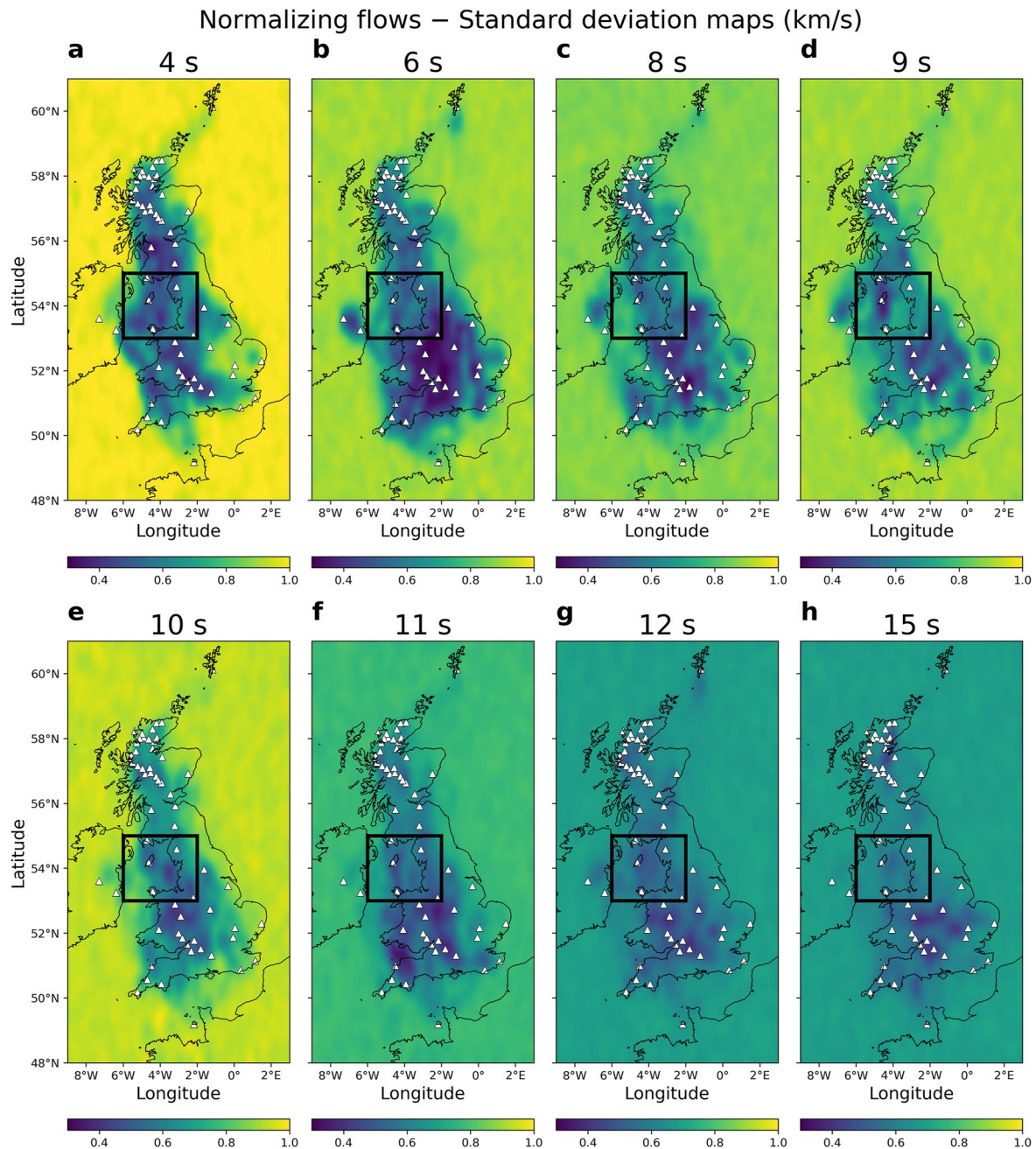


Figure 9. Standard deviation maps of the British Isles, interpolated between grid cell locations in the results obtained using normalizing flows at different periods between 4 and 15 s, each of which corresponds to one mean velocity map in Figure 8. All of the uncertainty maps are plotted using the same range for better comparison, and the corresponding period is shown above each map. The black boxes indicate the target region where we pick dispersion curves and perform depth inversion in the second step.

In order to include lateral spatial correlations in the inversion results, we use the 3D *rj*-MCMC algorithm of X. Zhang et al. (2018) to perform dispersion inversion in this step. The method parametrizes the subsurface velocity model with a 3D Voronoi tessellation, which varies both in shape and number of cells during the inversion. For a given 3D velocity model, the forward problem consists of extracting 1D shear velocity profiles over depth beneath each geographical point, and calculating a group velocity dispersion curve for that 1D structure using a modal approximation (Saito, 1988). Since we obtained different results from the three variational methods in the first step, we have three different sets of dispersion curve data for the second step. We therefore perform three independent dispersion inversions to examine the effect of using different algorithms and to reduce the

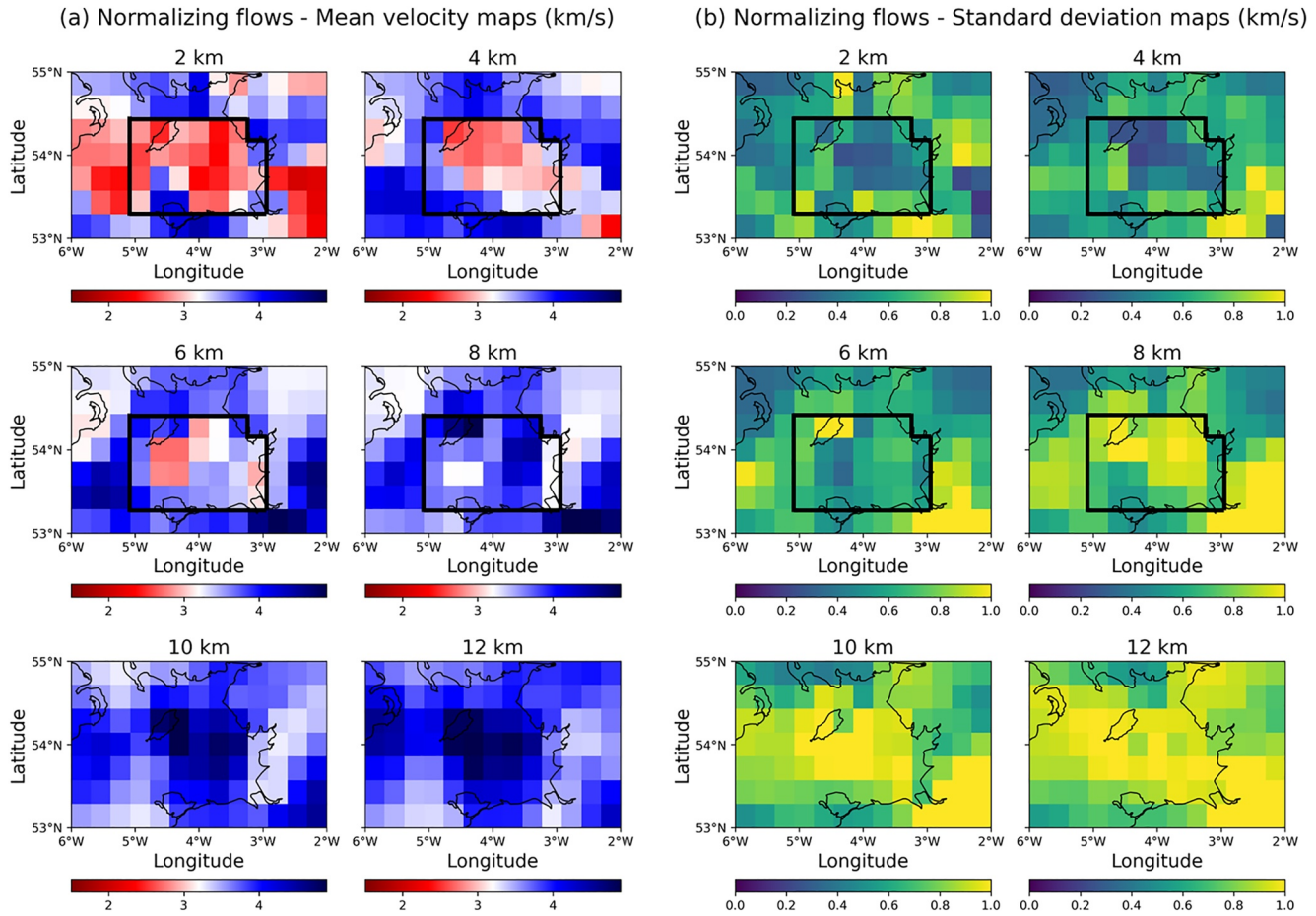


Figure 10. 3D reversible jump Markov chain Monte Carlo inversion results of shear wave velocity structure constrained by 91 dispersion curves picked from the 2D surface wave tomography results obtained using normalizing flows (within the black boxes in Figures 8 and 9). (a) Mean and (b) standard deviation maps of horizontal slices between 2 and 12 km depth.

algorithmic bias imposed on our final answer, similar to the approach taken in the synthetic example. For each inversion, the prior distribution is set to be a Uniform distribution on shear velocity in the subsurface between 0.5 and 6 km/s. The prior pdf on the number of Voronoi cells is selected to be a discrete Uniform distribution between 20 and 600 to address the complexity of the shear velocity structure beneath the East Irish Sea. The likelihood function is set to be a Gaussian distribution around the measured data. We perform each inversion by running 16 Markov chains with 3 million iterations, discarding the first 1 million samples from each chain as burn-in, and only retaining every 200th sample thereafter to calculate statistics of the posterior distribution and to apply interrogation theory. After completing the sampling process, we plot the posterior pdf of the number of Voronoi cells, as shown in Figure 7c. The posterior distribution on the number of cells is roughly distributed between 100 and 400, which lies well inside the boundaries of its prior distribution.

Considering that each posterior sample is defined using a different 3D Voronoi model parametrization, we first project all samples onto a regular grid of pixels. In this test, we define a 3D regular grid with a spacing of 0.33° in both latitude and longitude directions and 0.2 km in depth. We then compute the mean group velocity and standard deviation maps across the set of retained samples. Figures 10a and 10b show horizontal slices of the (pixelated) mean and uncertainty maps of the dispersion inversion results between 2 and 12 km depth, from the inversion result using dispersion data from normalizing flows (Figures 8 and 9). The average shear velocity increases with depth, and the uncertainty also increases since the resolution of Love wave data is lower in the deeper Earth. Again, in Figure 10 we observe similar features compared to those represent by Galetti et al. (2017), which proves the credibility of our results.

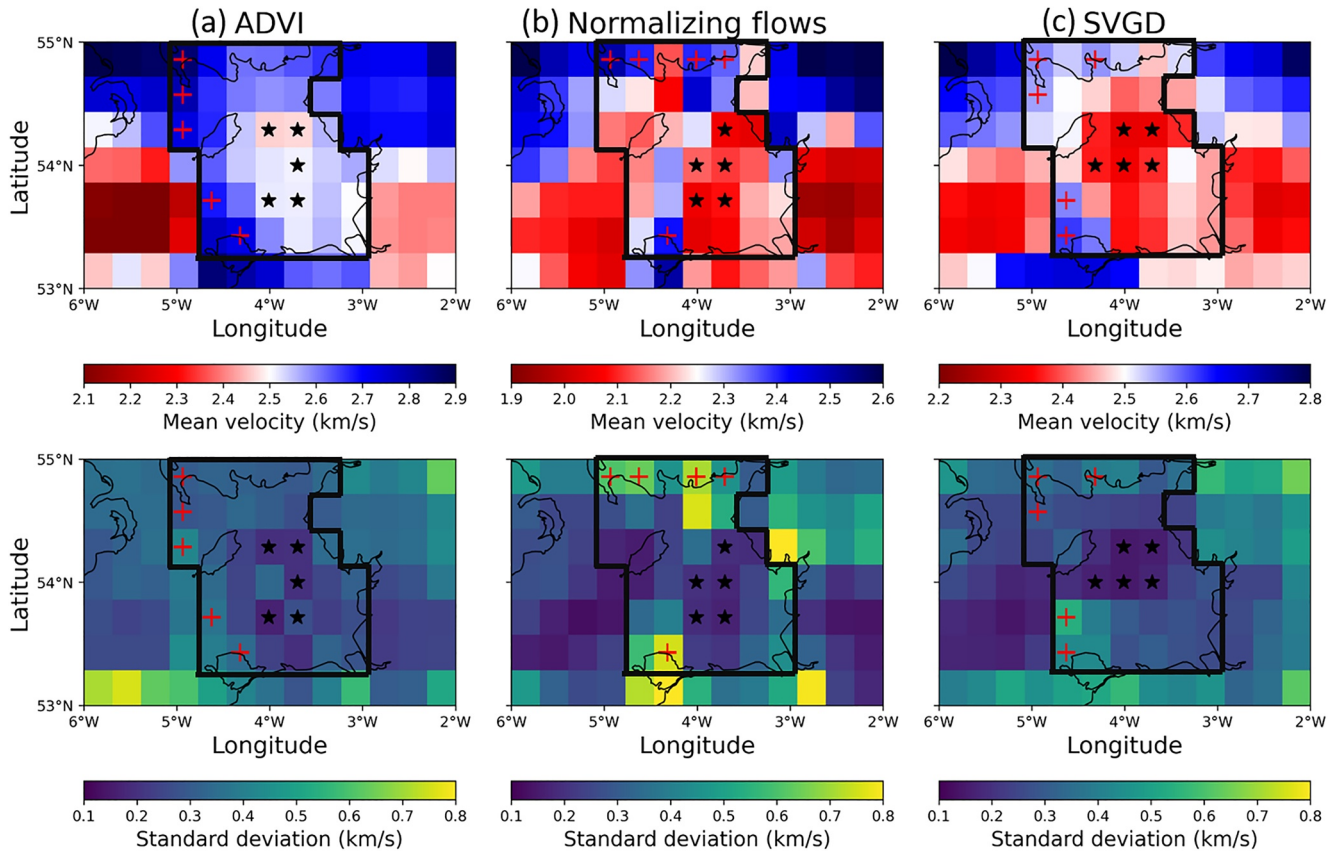


Figure 11. Mean (top row) and uncertainty (bottom row) maps of the top cell (from 0 to 200 m) of 3D shear wave velocity inversion results using dispersion curve data constructed from 2D tomography results obtained using (a) automatic differential variational inference (ADVI), (b) normalizing flows, and (c) Stein variational gradient descent (SVGd). In each figure, the black box displays the region where we calculate the area of the sedimentary basins. Black stars and red crosses are used to define the best threshold to discriminate low from high velocities with minimal bias.

From the mean velocity maps in Figure 10a, we can observe a low velocity structure beneath the East Irish Sea down to about 8 km depth, which is interpreted to be the East Irish Sea sedimentary basins in previous studies (Galetti et al., 2017; Mellett et al., 2015). Based on the three inversion results, we attempt to answer scientific questions about these sedimentary basins using the interrogation procedure tested above.

4.2. Estimating the Area of the East Irish Sea Basins in the Shallow Subsurface

We first estimate the area of the East Irish Sea sedimentary basins in the shallow subsurface using the top cell of the 3D inversion results which extends from surface down to 200 m depth. Figure 11 displays the top cell of the three inversion results. From left to right, each column stands for the average velocity (top row) and uncertainty (bottom row) maps of the inversion results using dispersion curves picked from 2D tomographic results obtained using (a) ADVI, (b) normalizing flows, and (c) SVGD (the three variational methods used in the first step only provide different dispersion curves for the second step, and we use the same 3D rj-MCMC algorithm for all depth inversions in the second step).

The geological structure beneath the Irish Sea can be divided into a number of bedrock basins representing depositional zones for the bedrock formations. The largest basins are Triassic in age and comprise the East Irish Sea basins (around 5°W–3°W and 53.3°N–55°N; Mellett et al., 2015). Thus, we pose a question: *what is the area of the East Irish Sea basins at this depth?* We have a reference answer to this question which is estimated from a shallow subsurface geological survey (1.12×10^4 km² estimated from Mellett et al., 2015) and which enables us to validate interrogation theory with real data.

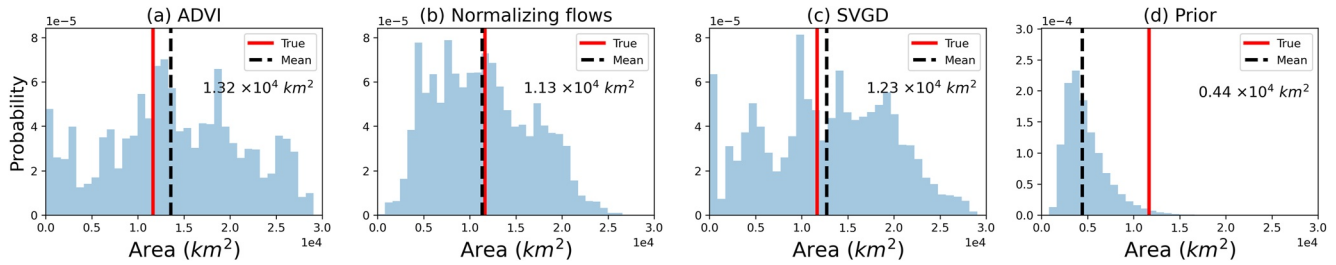


Figure 12. Posterior target functions for the area of the East Irish Sea basins at the shallow subsurface obtained from (a) automatic differential variational inference (ADVI), (b) normalizing flows, (c) Stein variational gradient descent (SVGD), and (d) prior distribution, respectively. In each figure, the red line denotes the reference answer to this question ($1.12 \times 10^4 \text{ km}^2$) estimated from surface geology (Mellett et al., 2015), and the dashed black line denotes the mean value of each histogram, which is also displayed by the number below the legend.

It is known that sedimentary basins often have lower velocities compared to their surrounding regions, and we have reasonably low uncertainties on the velocities of the near surface structure. Our question is therefore equivalent to estimating the area of the continuous low velocity body from the horizontal slice of the inversion results extending from the surface to 200 m depth. We apply exactly the same procedure as we implemented in the synthetic examples above to find the optimal answer. We first define a mask, as marked by the black boxes in Figure 11, meaning that we only consider the seismic velocity information inside the mask. The North, East, and South boundaries of the mask are determined by the coastline of mainland Britain, whereas the West boundary is defined based on the bedrock geology beneath the Irish Sea (Mellett et al., 2015). We select some points that are likely to belong to the East Irish Sea sedimentary basins (black stars in Figure 11), and another set of points that are highly likely to be outside the basins (red crosses in Figure 11). Given those grid cells, we calculate the best velocity threshold that discriminates low from high velocities with minimal bias using the same data-driven method as used in the synthetic test.

Similarly, we define our target function $T(\mathbf{m}|f(\mathbf{m}), C, Q)$ as the area of the largest continuous low velocity body inside the mask, and calculate the target function for each posterior sample from each algorithm. Figures 12a–12c display the posterior distributions of the target function calculated using the inversion results from ADVI, normalizing flows, and SVGD. In each figure, the mean value of the posterior target function (the optimal answer considering only each individual algorithm) is denoted by the dashed black line as well as the number below the legend, and the reference answer ($1.12 \times 10^4 \text{ km}^2$ estimated from Mellett et al., 2015) is denoted by the red line in each figure.

Given the forward function $f(\mathbf{m})$ used in the second inversion step, we define prior probabilities $p(C|f(\mathbf{m}))$ for different algorithms. We assign $p(C|f(\mathbf{m}))$ as 0.30 for ADVI and 0.35 for normalizing flows and SVGD (where these different algorithms were used for 2D surface wave tomography). The reason we only downweight ADVI slightly is that in this example, the role of these three methods is only to provide different data sets (mean and uncertainty values for dispersion curves) used in the second step depth inversion, in which we use the same algorithm: 3D rj-McMC. Previous studies (Zhang & Curtis, 2020a; Zhao et al., 2021) and the synthetic examples above have shown that ADVI can provide an accurate mean model but a biased uncertainty result; that is the dispersion curves (the observed dataset for the second step) constructed by ADVI would have accurate mean values but inaccurate data uncertainty estimates. We treat these inaccurate data errors as additional unknowns and adjust their values adaptively and hierarchically by a scaling value during 3D Rj-McMC inversion (Bodin et al., 2012; Galetti et al., 2017; X. Zhang et al., 2018), so the absolute data uncertainty level of the dispersion curves should have a far less effect on inversion results. By using Equation 3, we calculate the final optimal answer that considers the effect of different algorithms: $1.22 \times 10^4 \text{ km}^2$, which provides reasonable accuracy compared to the reference value for this question derived from the geological study ($1.12 \times 10^4 \text{ km}^2$ —Mellett et al., 2015).

We note that in Figures 12a–12c, the three posterior target functions span a very broad range (even the entire answer space from 0 to $3.0 \times 10^4 \text{ km}^2$ that is close to the total area of the defined mask), and the optimal answer we obtained also appears to be close to the mean value of the upper and lower bounds of the answer space ($1.5 \times 10^4 \text{ km}^2$). In principle one might argue that this is because the surface wave data used in this example (from 4 to 15 s period) are relatively insensitive to the near surface at a depth of up to 200 m; hence the posterior

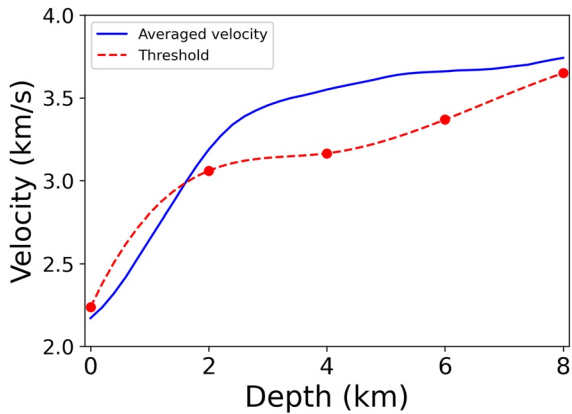


Figure 13. Mean velocity values at different depths from the surface to 8 km (blue line) and the optimal depth-dependent threshold curve to discriminate low from high velocity values with minimal bias (dashed red line).

samples may not be well constrained by the data, leading to a broadly distributed set of target function values which happen to have the same mean as the true answer. To investigate, we apply the same interrogation procedure using the same velocity threshold as above, to 2 million samples drawn from the Uniform prior distribution, and display the histogram of the calculated target function in Figure 12d. Obviously, the posterior target distributions and the optimal answers obtained from the three inversion results in Figures 12a–12c are significantly more informative than that estimated from the prior probability distribution which gives an extremely poor answer for the area of sediment. This shows that while it is true that the uncertainty on the final answer is high, the surface wave data are certainly far more informative than the answer that could be obtained from our prior information alone.

Since interrogation theory provides an optimal answer that is close to the answer obtained from an entirely different method based on interpreting surface geology, we have increased confidence in the result. This example as well as the synthetic tests therefore go some way toward validating interrogation theory as a practical method to answer scientific questions. In the next section, we apply the theory to answer a real-world scientific question where we do not know the true answer, and nor do we have any estimate based on independent data.

4.3. Estimating the Volume of the East Irish Sea Basins

We wish to answer a 3D volume-type question about the true Earth: *what is the total volume of the offshore East Irish Sea sedimentary basins?* This type of question may be of interest when performing mass balancing in tectonic or basin reconstructions, and questions of similar type arise in applied geoscience when assessing the volume of subsurface ore resources or fluid reservoirs. In this example we need to define a 3D mask inside which we calculate the volume of the basins. As displayed by the black boxes in Figures 10a and 10b, we define such a 3D mask with fixed shape in the depth direction from the surface down to 8 km depth to fully encompass the offshore sediments while excluding most of the land. In the horizontal direction, the boundaries of the mask are defined based on the coastline of mainland Britain as well as on the inversion results in Figure 10.

The target function of this 3D example should account for the volume of the low velocity bodies inside the mask, since sedimentary basins often have relatively lower velocities compared to the surrounding regions. In contrast to 2D cases above where we used a fixed threshold to discriminate low from high velocities, we now need threshold values that vary with depth to allow for the significant velocity changes that occur between different depths due to pressure and temperature increases. We use the following method to obtain such depth-dependent threshold values. First, we calculate five independent velocity threshold values at five fixed depths of 0 (surface), 2, 4, 6, and 8 km respectively, using exactly the same data-driven method as what we did in the 2D examples, and the obtained optimal threshold values are displayed by the red dots in Figure 13. We further interpolate between these five points to obtain the dashed red line in Figure 13. Each velocity value on this line is used as the optimal depth-dependent threshold that discriminates low from high velocities at the corresponding depth. The blue line in Figure 13 shows the average velocity value at different depths from the surface to 8 km. Although these two curves are not exactly the same (and there is no reason why they should be), they present a similar feature of velocity increasing versus depth, which increases our confidence in the obtained depth-dependent threshold curve.

Given the obtained depth-dependent threshold curve, we classify every pixel inside the 3D mask as a low or high velocity grid cell, retain low velocity pixels and find the continuous low velocity bodies. In contrast to the 2D cases where we treat the largest continuous low velocity body as the target function, we need to consider additional geological prior information when defining the target function for this 3D question. To illustrate, Figure 14 presents vertical slices of one posterior sample drawn from the 3D inversion results. The top row shows the depth slice at 53.67°N latitude and the bottom row shows the vertical section at 4.33°W longitude. The two depth slices of this posterior sample are shown in Figure 14a, and the same slices after applying the 3D mask are displayed in Figure 14b. By comparing each velocity value with the depth-dependent threshold curve, we retain low velocity

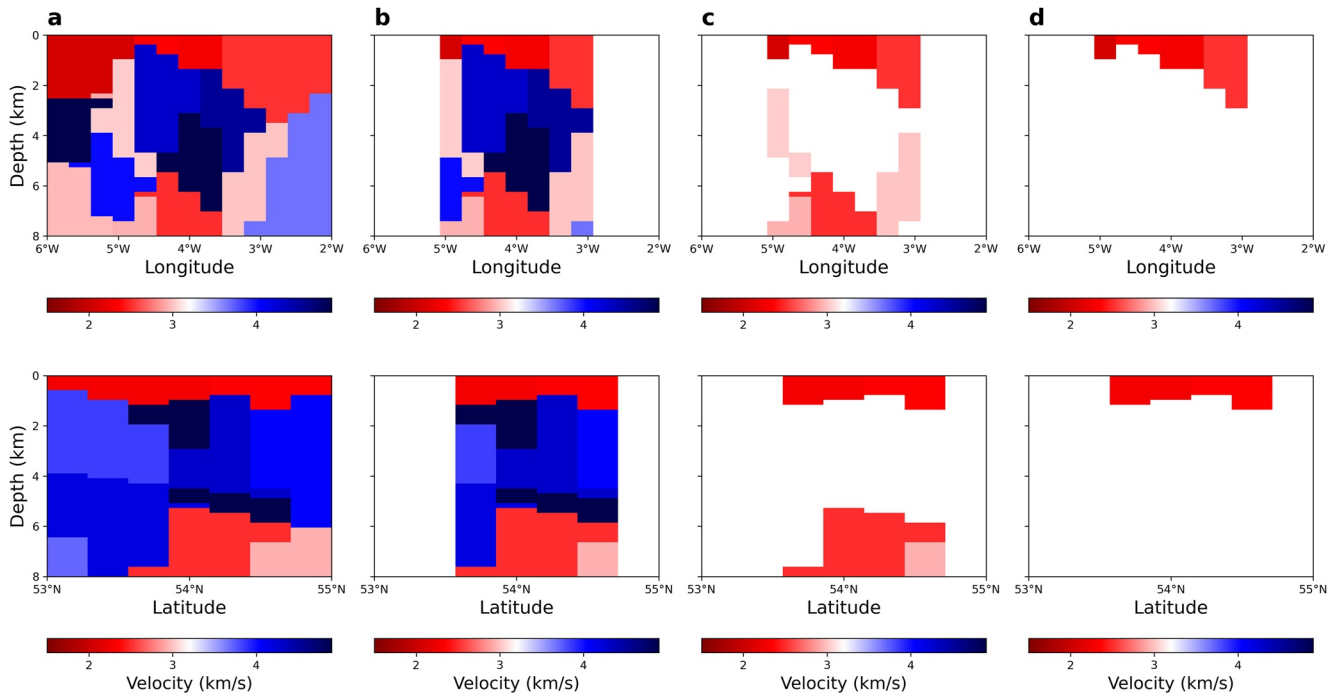


Figure 14. Vertical sections of a posterior sample drawn from the inversion results. The top row shows the vertical section at 53.67°N latitude and the bottom row shows that at 4.33°W longitude. (a) Two vertical slices of this posterior sample. (b) The same vertical slices as in (a) after applying the 3D mask. (c) Two continuous low velocity bodies classified by the depth-dependent threshold curve. (d) The largest continuous low velocity body that starts from surface, whose volume is treated as the target function of this posterior sample.

pixels and obtain two continuous low velocity bodies (Figure 14c). Given that we seek to estimate the volume of sedimentary basins, and considering that those sedimentary basins are often assumed to exist at least at the surface rather than only in deeper parts of the crust, we define the target function as the largest continuous low velocity body that starts from the surface (in other words, for each posterior sample we strictly require the low velocity body to exist at the surface, otherwise we assign that this sample has zero basin volume). Therefore we interpret the upper low velocity body as the sedimentary basins of interest (shown in Figure 14d) and calculate its volume as the target function of this posterior sample, even though the lower one is larger.

We calculate this target function for each posterior sample obtained from ADVI, normalizing flows, and SVGD, and display their posterior target histograms in Figure 15. The mean value of each posterior histogram represents the optimal answer estimated from each corresponding algorithm, which is denoted by the black dashed line and

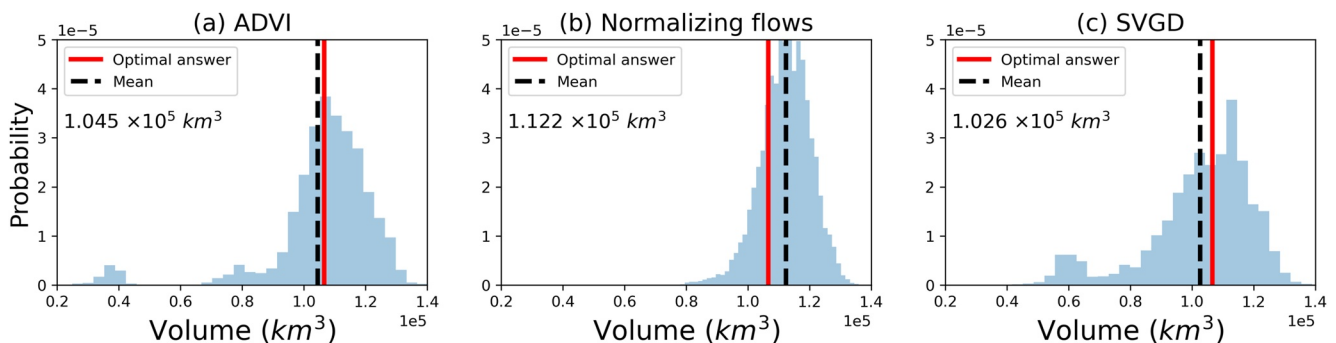


Figure 15. Posterior target functions for the volume of the East Irish Sea basins obtained from (a) automatic differential variational inference (ADVI), (b) normalizing flows, and (c) Stein variational gradient descent (SVGD), respectively. In each figure, the dashed black line denotes the posterior mean value of each algorithm, which is also displayed by the number below each legend, and the red line denotes the final estimated answer to this question ($1.065 \times 10^5 \text{ km}^3$).

the number below the legend in each figure. We substitute those values and the 3 prior probabilities $p(C|f(\mathbf{m}))$ into Equation 3, and obtain the final estimated answer to our question: $1.065 \times 10^5 \text{ km}^3$ (the red lines in Figure 15).

5. Discussion

We used interrogation theory to answer real-world, unanswered scientific questions about the Earth based on Bayesian inversion results represented by posterior probability distributions. Previously, similar questions were usually answered by interpreting mean or maximum likelihood models directly. In the synthetic example, we have proved that direct interpretation of the mean model alone provides an inaccurate answer, especially under a coarse model parametrization. The true Earth has infinitely fine structure, whereas we often use a relatively coarser parametrization to reduce the dimensionality of the inversion problem. It is therefore likely that the answer obtained in this way is always biased at some level. On the other hand, the examples presented above show that the optimal answer obtained from interrogation theory is very close to the true (reference) answer, despite the relatively coarse model parametrization (the grid size) employed.

The above result arises because the target function $T(\mathbf{m}|f(\mathbf{m}), C, Q)$, which projects model parameter \mathbf{m} into target space \mathbb{T} where the question can be answered directly, is applied stochastically. In the synthetic example, consider a fixed pixel that spans the boundary of the true velocity anomaly. In some samples it is classified as part of the low velocity anomaly by the defined target function (suppose we label those pixels as 1), while in other samples it is not (we label them as 0). By applying Equation 3, we account for the posterior mean of those labels, resulting in a fraction between [0, 1], which denotes the probability that this pixel belongs to the low velocity anomaly. For comparison, if we only interpret the mean model (or any other single model) alone, this same pixel always either belongs or does not belong to the low velocity anomaly, so it always contributes either 1 or 0. As a result, the effective resolution of the answer obtained from interrogation theory can be much higher than might be apparent from the grid cell size alone, since we consider all of the posterior samples together in a statistical manner. Thus the answer is still accurate even when using a coarser parametrization as observed in Supporting Information S1 associated with this paper.

Bayesian nonlinear inversion is many times more expensive than linearized inversion, especially for high dimensional problems due to the curse of dimensionality (Curtis & Lomax, 2001). Typically geophysicists only present, publish, and use a small amount of the statistical information obtained from Bayesian inversion results, such as mean and point-wise standard deviations; most of the valuable information within the posterior pdf is discarded, which can introduce errors and biases when answering questions. This paper shows that interrogation theory provides a way to make use of all posterior samples obtained from Bayesian inversion, in a way that gives answers of improved accuracy. This goes some way to justifying the computational expense of solving inverse problems nonlinearly and probabilistically.

We considered the effect of different computational inversion algorithms C , and combined them to calculate optimal answers (Equation 3). Thus, the uncertainty caused by the use of any single algorithm was taken into account and the bias of the obtained answer was reduced. On the other hand, all of the above examples only used a single forward function $f(\mathbf{m})$, the fast marching method (together with a modal approximation for the 3D example) to map model parameter \mathbf{m} into the corresponding data \mathbf{d} . Future improvements in interrogation applications might focus on involving different forward models to answer area-type (or volume-type) questions, for example, using full wave simulators as the forward model and using full waveform inversion to solve Bayesian inverse problems (Gebraad et al., 2020; Zhang & Curtis, 2020b, 2021), such that we can reduce the uncertainty caused by different model-data relationships.

In Equation 3, we translate the uncertainty from inversion results to the answer space by calculating the posterior distribution of the target function as shown in Figures 6, 12, and 15. Following Arnold and Curtis (2018) we obtain the statistically unbiased estimator of our answer by calculating the average value of each posterior histogram, which is the optimal answer $a_{f(\mathbf{m}),C}^*$ for each specific forward model $f(\mathbf{m})$ and algorithm C . The final optimal answer is obtained by taking a weighted sum of each $a_{f(\mathbf{m}),C}^*$. This provides a single estimate of the answer. Additional uncertainty in the answer could arise from the assignment of the weights assigned to each algorithm since these were assigned essentially by an informal expert elicitation process (where the authors were the experts). Polson and Curtis (2010) showed that expert elicitation can be a biased process in itself, but that if care is taken then uncertainties on elicited quantities can also be obtained. If we wish to quantify uncertainty

in the final answer caused by different algorithms and forward models, we may therefore replace the two prior values $p(\mathbf{f}(\mathbf{m}))$ and $p(C\mathbf{f}(\mathbf{m}))$ by two random variables with the elicited probability distributions: the output of Equation 3 then becomes a posterior distribution over the final answer. In this way we are able to incorporate uncertainty about the performance of different models and algorithms into the final answer.

Prior information is often critical in order to define a reasonable target function. In the synthetic example we defined the largest continuous low velocity body to be the low velocity anomaly of interest rather than simply including all of the low velocity bodies inside the mask. In the field data test, we interpreted sedimentary basins as low velocity bodies considering that basins often have relatively lower velocities compared to their surrounding rocks, and further interpreted the largest continuous low velocity body that starts from the surface to be the 3D basins of interest since these basins have been observed in the near surface geologically. The definition of the target function may be more or less subjective in different applications, but this is how one incorporates realistic geological prior information into the target function. Geological information is itself mainly based on knowledge from experts, hence is affected by subjective choices (Bond et al., 2007, 2012; Curtis, 2012; Polson & Curtis, 2010). The application of interrogation theory in this paper tries to reduce some of the bias that would be imposed by individuals who often use a single algorithm or method, but we still need (subjective) expertise to make the procedure geologically reasonable. Therefore, the target function will always be more accurate if we consider more realistic prior information, and thus will provide a more reliable answer.

In 3D Rj-McMC inversion, we first projected 3D Voronoi-tessellated models onto a regular gridded system, such that we can compute some statistics of the posterior distribution (the average model and point-wise standard deviations). We used these regular gridded samples to calculate their target function values. As an alternative we could have performed the target function calculations directly on the Voronoi-tessellated models, taking care to account for cell volumes so that the estimated threshold values that discriminate low and high velocities remain unbiased.

In this paper, we explicitly tested two different experimental designs: a circular design used in the synthetic example and a fixed receiver network used in the field data test. In both cases, we used interrogation theory to find the best answer a^* . In addition, in the second step of the 3D inversion, we used three different dispersion data sets picked from three variational tomographic results. These three data sets can also be viewed as data obtained from three different “experimental designs.” Therefore, the posterior target functions shown in Figure 15 can be interpreted as interrogation results obtained from three different experimental designs, which provided similar results in answer space.

In reality, it is common that the (predefined) design used to collect data is not the optimal one for the question posed because when networks are established it is always difficult to define a design that can best answer all questions that may be of interest in future. Interrogation theory also provides a methodology to solve design problems to create an experiment that optimizes information on one or more questions (Arnold & Curtis, 2018). For a given question, we seek the design that provides answers with the highest expected utility (before collecting data). For each design from a group of candidate designs, we calculate the utility value averaged over a representative set of all possible data sets observable under that design. The optimal design is the one that maximizes this expected utility value. To solve a design problem, in principle we therefore need to solve thousands of inverse problems (number of candidate designs \times number of possible datasets for one design), which is far more expensive than a single probabilistic tomographic problem (although simplifications can be made which reduce this calculation significantly (e.g., Shewry & Wynn, 1987)).

For real-world applications, it is possible that our ultimate question may not be addressed clearly within one interrogation procedure. To better answer the original question, a set of new questions are usually posed to provide more background knowledge, and a sequential interrogation process is required until a satisfactory answer is obtained. For more details about sequential interrogation, we suggest readers refer to Arnold and Curtis (2018).

In the field data test, we used interrogation theory to find the optimal volume of the East Irish Sea sedimentary basin. To our limited knowledge, this is the first time that geophysicist tried to estimate the volume of a basin directly from geophysical inversion results. In recent years, carbon capture and storage (CCS) has become a key technology for the provision of energy with low carbon dioxide emissions. The East Irish Sea basins studied in this paper host a large carbon dioxide storage potential and represent a prospective area for CCS in the western

UK (Gamboa et al., 2016, 2019). The inversion results for the shear-velocity structure as well as the estimated basin volume can be used to as background information for future research on CCS beneath the East Irish Sea.

Interrogation theory as presented in Arnold and Curtis (2018) appears to be highly structured and formalized. One purpose of this paper is to translate the theory into useable form, and to provide a concrete example of answering a specific type of question. One of the main theoretical advances of Arnold and Curtis (2018) was to introduce the target function in order to allow utilities to be defined in a simpler, more tractable form, even when a variety of parametrizations and forward functions are considered. A key revelation from our examples above is that much of the skill and work involved in answering real-world questions may be spent specifying prior weights for different algorithms and forward models and defining reasonable target functions in a clear and unbiased manner. We hope to use interrogation theory to answer a wide range of real-world scientific questions in future studies.

6. Conclusion

In this paper, we use interrogation theory to answer a specific type of question about the Earth: to estimate the shape, area, or volume of a subsurface structure by interrogating probabilistic Bayesian tomographic results. We establish an interrogation procedure by using a 2D synthetic example. By considering the effect of different computational algorithms, we reduce the bias of the optimal answer and obtain an accurate estimation of the question. The results using different parametrizations show that the same question can be answered accurately even on a relatively coarse grid, which reduces the computational cost of Bayesian inversion by orders of magnitude. We further apply interrogation theory to answer realistic questions about the East Irish Sea basins. The first application to estimate the horizontal area of the shallow part of the basins validates the theory, as the answer coincides to within 10% of that obtained from surface geological survey mapping. Finally, we use the method to estimate the total volume of the East Irish Sea basins for which no previously published answer exists. The theory established here is quite general, and can be applied to find answers for many other real-world scientific questions.

Data Availability Statement

Traveltime data associated with both the synthetic and the field data tests are available at Edinburgh DataShare (<https://datashare.ed.ac.uk/handle/10283/4400>). Software used for the three variational methods as well as the 2D McMC can be found at PyMC3 website (<https://docs.pymc.io/en/v3/>, Salvatier et al., 2016). 3D Rj-McMC code is available at <https://github.com/xin2zhang/MCTomo> (X. Zhang et al., 2018).

Acknowledgments

The authors wish to thank Erica Galetti for providing the traveltime data used in the field data test, and thank PyMC3 developers for providing software used in this paper. They thank the Edinburgh Imaging Project (EIP) sponsors (BP and TotalEnergies) for supporting this research. For the purpose of open access, the authors have applied a Creative Commons Attribution (CC BY) license to any Author Accepted Manuscript version arising.

References

- Arnold, R., & Curtis, A. (2018). Interrogation theory. *Geophysical Journal International*, 214(3), 1830–1846. <https://doi.org/10.1093/gji/ggy248>
- Bishop, C. M. (2006). *Pattern recognition and machine learning*. Springer.
- Blei, D. M., Kucukelbir, A., & McAuliffe, J. D. (2017). Variational inference: A review for statisticians. *Journal of the American Statistical Association*, 112(518), 859–877. <https://doi.org/10.1080/01621459.2017.1285773>
- Bloem, H., Curtis, A., & Maurer, H. (2020). Experimental design for fully nonlinear source location problems: Which method should i choose? *Geophysical Journal International*, 223(2), 944–958. <https://doi.org/10.1093/gji/ggaa358>
- Bodin, T., & Sambridge, M. (2009). Seismic tomography with the reversible jump algorithm. *Geophysical Journal International*, 178(3), 1411–1436. <https://doi.org/10.1111/j.1365-246x.2009.04226.x>
- Bodin, T., Sambridge, M., Rawlinson, N., & Arroucau, P. (2012). Transdimensional tomography with unknown data noise. *Geophysical Journal International*, 189(3), 1536–1556. <https://doi.org/10.1111/j.1365-246x.2012.05414.x>
- Bond, C. E., Gibbs, A. D., Shipton, Z. K., & Jones, S. (2007). What do you think this is? “Conceptual uncertainty” in geoscience interpretation. *Geological Society of America Today*, 17(11), 4. <https://doi.org/10.1130/gsat01711a.1>
- Bond, C. E., Lunn, R., Shipton, Z., & Lunn, A. (2012). What makes an expert effective at interpreting seismic images? *Geology*, 40(1), 75–78. <https://doi.org/10.1130/g32375.1>
- Chaloner, K., & Verdinelli, I. (1995). Bayesian experimental design: A review. *Statistical Science*, 273–304. <https://doi.org/10.1214/ss/1177009939>
- Curtis, A. (2012). The science of subjectivity. *Geology*, 40(1), 95–96. <https://doi.org/10.1130/focus012012.1>
- Curtis, A., Gerstoft, P., Sato, H., Snieder, R., & Wapenaar, K. (2006). Seismic interferometry—Turning noise into signal. *The Leading Edge*, 25(9), 1082–1092. <https://doi.org/10.1190/1.2349814>
- Curtis, A., & Lomax, A. (2001). Prior information, sampling distributions, and the curse of dimensionality. *Geophysics*, 66(2), 372–378. <https://doi.org/10.1190/1.1444928>
- Devilee, R., Curtis, A., & Roy-Chowdhury, K. (1999). An efficient, probabilistic neural network approach to solving inverse problems: Inverting surface wave velocities for Eurasian crustal thickness. *Journal of Geophysical Research*, 104(B12), 28841–28857. <https://doi.org/10.1029/1999jb900273>
- Earp, S., & Curtis, A. (2020). Probabilistic neural network-based 2D travel-time tomography. *Neural Computing & Applications*, 32(22), 17077–17095. <https://doi.org/10.1007/s00521-020-04921-8>

- Fichtner, A., & Simuté, S. (2018). Hamiltonian Monte Carlo inversion of seismic sources in complex media. *Journal of Geophysical Research: Solid Earth*, 123(4), 2984–2999. <https://doi.org/10.1002/2017jb015249>
- Fichtner, A., Zunino, A., & Gebrärd, L. (2019). Hamiltonian Monte Carlo solution of tomographic inverse problems. *Geophysical Journal International*, 216(2), 1344–1363. <https://doi.org/10.1093/gji/ggy496>
- Galetti, E., Curtis, A., Baptie, B., Jenkins, D., & Nicolson, H. (2017). Transdimensional love-wave tomography of the British Isles and shear-velocity structure of the East Irish Sea basin from ambient-noise interferometry. *Geophysical Journal International*, 208(1), 36–58. <https://doi.org/10.1093/gji/ggw286>
- Galetti, E., Curtis, A., Meles, G. A., & Baptie, B. (2015). Uncertainty loops in travel-time tomography from nonlinear wave physics. *Physical Review Letters*, 114(14), 148501. <https://doi.org/10.1103/physrevlett.114.148501>
- Gamboa, D., Williams, J. D., Bentham, M., Schofield, D. I., & Mitchell, A. C. (2019). Application of three-dimensional fault stress models for assessment of fault stability for CO₂ storage sites. *International Journal of Greenhouse Gas Control*, 90, 102820. <https://doi.org/10.1016/j.ijggc.2019.102820>
- Gamboa, D., Williams, J. D. O., Kirk, K., Gent, C. M., Bentham, M., & Schofield, D. I. (2016). The Collyhurst Sandstone as a secondary storage unit for CCS in the East Irish Sea basin (UK) *AGU fall meeting abstracts* (Vol. 2016, pp. PA23C–2242).
- Gebrärd, L., Boehm, C., & Fichtner, A. (2020). Bayesian elastic full-waveform inversion using Hamiltonian Monte Carlo. *Journal of Geophysical Research: Solid Earth*, 125(3), e2019JB018428. <https://doi.org/10.1029/2019jb018428>
- Guest, T., & Curtis, A. (2009). Iteratively constructive sequential design of experiments and surveys with nonlinear parameter-data relationships. *Journal of Geophysical Research*, 114(B4), B04307. <https://doi.org/10.1029/2008jb005948>
- Hastings, W. K. (1970). Monte Carlo sampling methods using Markov chains and their applications. *Biometrika*, 57(1), 97–109. <https://doi.org/10.1093/biomet/57.1.97>
- Jackson, D. D. (1972). Interpretation of inaccurate, insufficient and inconsistent data. *Geophysical Journal International*, 28(2), 97–109. <https://doi.org/10.1111/j.1365-246x.1972.tb06115.x>
- Julian, B., & Gubbins, D. (1977). Three-dimensional seismic ray tracing. *Journal of Geophysics*, 43(1), 95–113.
- Käufli, P., Valentine, A. P., de Wit, R. W., & Trampert, J. (2016). Solving probabilistic inverse problems rapidly with prior samples. *Geophysical Journal International*, 205(3), 1710–1728. <https://doi.org/10.1093/gji/ggw108>
- Käufli, P., Valentine, A. P., O’Toole, T. B., & Trampert, J. (2014). A framework for fast probabilistic centroid-moment-tensor determination—Inversion of regional static displacement measurements. *Geophysical Journal International*, 196(3), 1676–1693. <https://doi.org/10.1093/gji/ggt473>
- Khoshkholgh, S., Zunino, A., & Mosegaard, K. (2021). Informed proposal Monte Carlo. *Geophysical Journal International*, 226(2), 1239–1248. <https://doi.org/10.1093/gji/ggab173>
- Kucukelbir, A., Tran, D., Ranganath, R., Gelman, A., & Blei, D. M. (2017). Automatic differentiation variational inference. *Journal of Machine Learning Research*, 18(1), 430–474.
- Kullback, S., & Leibler, R. A. (1951). On information and sufficiency. *The Annals of Mathematical Statistics*, 22(1), 79–86. <https://doi.org/10.1214/aoms/1177729694>
- Liu, Q., & Wang, D. (2016). Stein variational gradient descent: A general purpose Bayesian inference algorithm. In *Advances in neural information processing systems* (pp. 2378–2386).
- Maurer, H., Curtis, A., & Boerner, D. E. (2010). Recent advances in optimized geophysical survey design. *Geophysics*, 75(5), 75A177–75A194. <https://doi.org/10.1190/1.3484194>
- Meier, U., Curtis, A., & Trampert, J. (2007). Fully nonlinear inversion of fundamental mode surface waves for a global crustal model. *Geophysical Research Letters*, 34(16), L16304. <https://doi.org/10.1029/2007gl030989>
- Mellett, C., Long, D., & Carter, G. (2015). Geology of the seabed and shallow subsurface: The Irish Sea. *British Geological Survey Commissioned Report CR/15/057* (pp. 1–42).
- Metropolis, N., Rosenbluth, A. W., Rosenbluth, M. N., Teller, A. H., & Teller, E. (1953). Equation of state calculations by fast computing machines. *The Journal of Chemical Physics*, 21(6), 1087–1092. <https://doi.org/10.1063/1.1699114>
- Metropolis, N., & Ulam, S. (1949). The Monte Carlo method. *Journal of the American Statistical Association*, 44(247), 335–341. <https://doi.org/10.1080/01621459.1949.10483310>
- Mosegaard, K., & Tarantola, A. (1995). Monte Carlo sampling of solutions to inverse problems. *Journal of Geophysical Research*, 100(B7), 12431–12447. <https://doi.org/10.1029/94jb03097>
- Nawaz, A., & Curtis, A. (2018). Variational Bayesian inversion (VBI) of quasi-localized seismic attributes for the spatial distribution of geological facies. *Geophysical Journal International*, 214(2), 845–875. <https://doi.org/10.1093/gji/ggy163>
- Nawaz, A., & Curtis, A. (2019). Rapid discriminative variational Bayesian inversion of geophysical data for the spatial distribution of geological properties. *Journal of Geophysical Research: Solid Earth*, 124(6), 5867–5887. <https://doi.org/10.1029/2018jb016652>
- Nawaz, A., Curtis, A., Shahraeeni, M. S., & Gerea, C. (2020). Variational Bayesian inversion of seismic attributes jointly for geological facies and petrophysical rock properties. *Geophysics*, 85(4), 1–78. <https://doi.org/10.1190/geo2019-0163.1>
- Nicolson, H., Curtis, A., & Baptie, B. (2014). Rayleigh wave tomography of the British Isles from ambient seismic noise. *Geophysical Journal International*, 198(2), 637–655. <https://doi.org/10.1093/gji/ggu071>
- Nicolson, H., Curtis, A., Baptie, B., & Galetti, E. (2012). Seismic interferometry and ambient noise tomography in the British Isles. *Proceedings of the Geologists’ Association*, 123(1), 74–86. <https://doi.org/10.1016/j.pgeola.2011.04.002>
- Polson, D., & Curtis, A. (2010). Dynamics of uncertainty in geological interpretation. *Journal of the Geological Society*, 167(1), 5–10. <https://doi.org/10.1144/0016-76492009-055>
- Rawlinson, N., & Sambridge, M. (2004). Wave front evolution in strongly heterogeneous layered media using the fast marching method. *Geophysical Journal International*, 156(3), 631–647. <https://doi.org/10.1111/j.1365-246x.2004.02153.x>
- Rezende, D. J., & Mohamed, S. (2015). *Variational inference with normalizing flows*. arXiv preprint arXiv:1505.05770.
- Saito, M. (1988). Disper80: A subroutine package for the calculation of seismic normal-mode solutions. *Seismological algorithms*, 293–319.
- Salvatier, J., Wiecki, T. V., & Fonnesbeck, C. (2016). Probabilistic programming in python using pymc3. *PeerJ Computer Science*, 2, e55. <https://doi.org/10.7717/peerj-cs.55>
- Shapiro, N. M., Campillo, M., Stehly, L., & Ritzwoller, M. H. (2005). High-resolution surface-wave tomography from ambient seismic noise. *Science*, 307(5715), 1615–1618. <https://doi.org/10.1126/science.1108339>
- Shewry, M. C., & Wynn, H. P. (1987). Maximum entropy sampling. *Journal of Applied Statistics*, 14(2), 165–170. <https://doi.org/10.1080/02664768700000020>
- Siahkoobi, A., Orozco, R., Rizzuti, G., Witte, P. A., Louboutin, M., & Herrmann, F. J. (2021). Fast and reliability-aware seismic imaging with conditional normalizing flows. In *Intelligent Illumination of the Earth*. KAUST, virtual.

- Siahkoohi, A., Rizzuti, G., & Herrmann, F. J. (2021). *Deep Bayesian inference for seismic imaging with tasks*. arXiv preprint arXiv:2110.04825.
- Siahkoohi, A., Rizzuti, G., Louboutin, M., Witte, P. A., & Herrmann, F. J. (2021). *Preconditioned training of normalizing flows for variational inference in inverse problems*. arXiv preprint arXiv:2101.03709.
- Singh, J., Tant, K. M., Curtis, A., & Mulholland, A. J. (2021). *Real-time super-resolution mapping of locally anisotropic grain orientations for ultrasonic non-destructive evaluation of crystalline material*. arXiv preprint arXiv:2105.09466.
- Tarantola, A. (2005). *Inverse problem theory and methods for model parameter estimation* (Vol. 89). SIAM.
- vanDen Berg, J., Curtis, A., & Trampert, J. (2003). Optimal nonlinear Bayesian experimental design: An application to amplitude versus offset experiments. *Geophysical Journal International*, 155(2), 411–421. <https://doi.org/10.1046/j.1365-246x.2003.02048.x>
- Wolpert, D. H., & Macready, W. G. (1997). No free lunch theorems for optimization. *IEEE Transactions on Evolutionary Computation*, 1(1), 67–82. <https://doi.org/10.1109/4235.585893>
- Zhang, C., Bütepage, J., Kjellström, H., & Mandt, S. (2018). Advances in variational inference. *IEEE Transactions on Pattern Analysis and Machine Intelligence*, 41(8), 2008–2026.
- Zhang, X., & Curtis, A. (2020a). Seismic tomography using variational inference methods. *Journal of Geophysical Research: Solid Earth*, 125(4), e2019JB018589. <https://doi.org/10.1029/2019jb018589>
- Zhang, X., & Curtis, A. (2020b). Variational full-waveform inversion. *Geophysical Journal International*, 222(1), 406–411. <https://doi.org/10.1093/gji/ggaa170>
- Zhang, X., & Curtis, A. (2021). Interrogating probabilistic inversion results for subsurface structural information. *Geophysical Journal International*, 229(2), 750–757. <https://doi.org/10.1093/gji/ggab496>
- Zhang, X., Curtis, A., Galetti, E., & De Ridder, S. (2018). 3-d Monte Carlo surface wave tomography. *Geophysical Journal International*, 215(3), 1644–1658. <https://doi.org/10.1093/gji/ggy362>
- Zhang, X., Nawaz, A., Zhao, X., & Curtis, A. (2021). An introduction to variational inference in geophysical inverse problems. *Advances in Geophysics*, 62, 73–140. <https://doi.org/10.1016/bs.agph.2021.06.003>
- Zhao, X., Curtis, A., & Zhang, X. (2021). Bayesian seismic tomography using normalizing flows. *Geophysical Journal International*, 228(1), 213–239. <https://doi.org/10.1093/gji/ggab298>